



Publication Year	2019
Acceptance in OA @INAF	2020-12-01T17:07:10Z
Title	Photometric Determination of the Mass Accretion Rates of Pre-main-sequence Stars. VI. The Case of LH 95 in the Large Magellanic Cloud
Authors	BIAZZO, Katia; BECCARI, GIACOMO; De Marchi, Guido; Panagia, Nino
DOI	10.3847/1538-4357/ab0f95
Handle	http://hdl.handle.net/20.500.12386/28612
Journal	THE ASTROPHYSICAL JOURNAL
Number	875



Photometric Determination of the Mass Accretion Rates of Pre-main-sequence Stars. VI. The Case of LH 95 in the Large Magellanic Cloud*

Katia Biazzo¹ , Giacomo Beccari² , Guido De Marchi³ , and Nino Panagia^{4,5}

¹ INAF—Osservatorio Astrofisico di Catania, Via Santa Sofia 78, I-95123 Catania, Italy; katia.biazzo@inaf.it

² European Southern Observatory, Karl-Schwarzschild-Str. 2, D-85748 Garching, Germany

³ European Space Research and Technology Centre, Keplerlaan 1, 2200 AG Noordwijk, The Netherlands

⁴ Space Telescope Science Institute, 3700 San Martin Drive, Baltimore, MD 21218, USA

⁵ Supernova Limited, OYV #131, Northsound Road, Virgin Gorda VG1150, Virgin Islands, UK

Received 2018 September 13; revised 2019 March 12; accepted 2019 March 12; published 2019 April 16

Abstract

We report on the accretion properties of low-mass stars in the LH 95 association within the Large Magellanic Cloud. Using noncontemporaneous wideband optical and narrowband H α photometry obtained with the *Hubble Space Telescope*, we identify 245 low-mass pre-main-sequence (PMS) candidates showing H α excess emission above the 4σ level. We derive their physical parameters, including effective temperatures, luminosities, masses (M_*), ages, accretion luminosities, and mass accretion rates (\dot{M}_{acc}). We identify two different stellar populations: younger than ~ 8 Myr with median $\dot{M}_{\text{acc}} \sim 5.4 \times 10^{-8} M_{\odot} \text{ yr}^{-1}$ (and $M_* \sim 0.15\text{--}1.8 M_{\odot}$) and older than ~ 8 Myr with median $\dot{M}_{\text{acc}} \sim 4.8 \times 10^{-9} M_{\odot} \text{ yr}^{-1}$ (and $M_* \sim 0.6\text{--}1.2 M_{\odot}$). We find that the younger PMS candidates are assembled in groups around Be stars, while older PMS candidates are uniformly distributed within the region without evidence of clustering. We find that \dot{M}_{acc} in LH 95 decreases with time more slowly than what is observed in Galactic star-forming regions (SFRs). This agrees with the recent interpretation, according to which higher metallicity limits the accretion process in both rate and duration due to higher radiation pressure. The $\dot{M}_{\text{acc}}\text{--}M_*$ relationship shows different behavior at different ages, becoming progressively steeper at older ages, indicating that the effects of mass and age on \dot{M}_{acc} cannot be treated independently. With the aim to identify reliable correlations between mass, age, and \dot{M}_{acc} , we used a multivariate linear regression fit between these parameters for our PMS candidates. The comparison between our results and those obtained in other SFRs of our Galaxy and the Magellanic Clouds confirms the importance of the metallicity for the study of the \dot{M}_{acc} evolution in clusters with different environmental conditions.

Key words: accretion, accretion disks – Magellanic Clouds – open clusters and associations: individual (LH95) – stars: formation – stars: pre-main sequence

Supporting material: machine-readable table

1. Introduction

In the current star formation paradigm of the magnetospheric accretion scenario, a central low-mass star grows in mass over time through accretion of material from a circumstellar disk of dust and gas funneled by the stellar magnetic field, assumed to be mostly dipolar (e.g., Camenzind 1990; Königl 1991). The accretion disk is then truncated by the stellar magnetosphere at a few stellar radii (see a recent review on accretion onto pre-main-sequence (PMS) stars by Hartmann et al. 2016). Reliable measurements of the rate at which mass from the circumstellar disk is transferred onto the central PMS star is therefore important for understanding the evolution of both the star and its disk and for tracing possible planetary formation and subsequent evolution. In particular, the study of how the mass accretion rate changes with time as a star approaches the main sequence (MS), how it depends on the mass of the forming star, and how it is affected by the metallicity and density of the parent cloud or the proximity of early-type stars is of particular interest.

Ground-based studies of Galactic nearby star-forming regions (SFRs) show a decrease of the mass accretion rate

(\dot{M}_{acc}) with time, from $\sim 9 \times 10^{-8} M_{\odot} \text{ yr}^{-1}$ at ~ 1 Myr to $\sim 6 \times 10^{-10} M_{\odot} \text{ yr}^{-1}$ at ~ 10 Myr with a power law $\dot{M}_{\text{acc}}^{-1.2}$ (e.g., Sicilia-Aguilar et al. 2010). This behavior is in line with the expected evolution of viscous disks (Hartmann et al. 1998; Mulders et al. 2017; Rosotti et al. 2017), but the spread of the data may exceed 2 dex at any given age. Such a scatter can be explained in part by the wide mass range covered by the observations, since the mass accretion rate also depends on the mass M_* of the forming star. While during the last 20 yr, several authors discussed the steepness of the one-power $\dot{M}_{\text{acc}}\text{--}M_*$ relation (see, e.g., Alcalá et al. 2014 and references therein), recently, observations have suggested that two different exponents for this relation at different mass regimes can better describe the data than a single power law (Fang et al. 2013; Alcalá et al. 2017; Manara et al. 2017), and this behavior resembles theoretical predictions (Vorobyov & Basu 2009). In particular, for $M_* > 0.2 M_{\odot}$, the mass accretion rate was found to scale with the power of $\sim 1.3\text{--}1.4$ of the stellar mass. These latter works claim the importance of modeling the self-gravity of the disks in the early evolution of the more massive systems, but also of other physical processes, such as that photoevaporation and planet formation during the lifetime of young stellar objects may lead to disk dissipation on different timescales depending on stellar mass (see Alcalá et al. 2017 and references therein).

* Based on observations made with the NASA/ESA *Hubble Space Telescope*, obtained from the Data Archive at the Space Telescope Science Institute, which is operated by the Association of Universities for Research in Astronomy, Inc., under NASA contract NAS 5-26555.

While potential systematic errors may contribute to the present uncertainty in the $\dot{M}_{\text{acc}}-M_*$ relation, one of the main limitations of the ground-based observations comes from the relatively paucity of available measurements. Indeed, most of the results so far obtained are based on the mass accretion rates of some hundred stars, all located in nearby Galactic SFRs, covering a limited range of ages ($\sim 0.5-20$ Myr) and with essentially solar metallicity (see, e.g., Muzerolle et al. 1998; Herczeg & Hillenbrand 2008; Antonucci et al. 2011; Rigliaco et al. 2011; Biazzo et al. 2012; Costigan et al. 2012; Fang et al. 2013; Alcalá et al. 2014). The origin of this limitation can be found in the methods used to measure \dot{M}_{acc} . Indeed, current techniques based on medium-high-resolution single-object spectroscopy or low-medium-resolution multi-object spectroscopy (or UV photometry) of nearby regions limit the number of objects and the distance to the regions that can be observed (e.g., because of crowding). To partially overcome these limitations, De Marchi et al. (2010) developed and tested a new method to reliably measure the mass accretion rate from photometry of the SN1987A field. This method, successfully applied to several regions of the Large Magellanic Cloud (LMC; Spezzi et al. 2012; De Marchi et al. 2017), Small Magellanic Cloud (SMC; De Marchi et al. 2011, 2013), and Milky Way (MW; Beccari et al. 2010, 2015; Zeidler et al. 2016), combines wideband V and I photometry with narrowband $H\alpha$ imaging to identify all stars with significant $H\alpha$ excess emission and derive from it the accretion luminosity (L_{acc}) and hence \dot{M}_{acc} for many hundreds of objects all at once.

Here we apply the same method to the young association LH 95. This region, first identified by Lucke & Hodge (1970), is one of the stellar aggregates located north of the LMC at $\alpha \sim 5^{\text{h}}37^{\text{m}}04^{\text{s}}.32$ and $\delta \sim -66^{\circ}22'00''.7$ in J2000. This group was recognized by Kontizas et al. (1994) as an association that is rather poor in total number of stars and low in density ($\sim 0.05-0.07 M_{\odot} \text{pc}^{-3}$). It is embedded in the bright H II region LH α 120/N 64C (Henize 1956), in an area situated to the northeast of the superbubble LMC 4. Lucke (1974) detected four early-type stars ($B - V \sim 0$) with $13 < V < 16$, while Kontizas et al. (1994) counted 15 blue stars and estimated a mean age of $2 \pm 1 \times 10^7$ yr for the region.

Most recently, Gouliermis et al. (2002) determined a diameter slightly higher than about $2'$ for LH 95. From the $R - H\alpha$ color index versus the $B - V$ color index, they identified a central cluster of four Be stars that strongly determine the H II emissivity in an area of $\sim 4'.1 \times 5'.3$. They estimated a reddening of 0.1–0.2 mag in $B - V$ color and an age as young as ~ 8 Myr within the cluster and older than ~ 50 Myr in the field. They discussed the possibility that LH 95 is not a large mass-segregated system but rather a small young system. Studies on the initial mass function from the high-mass ($\sim 70 M_{\odot}$) down to the subsolar ($\sim 0.4 M_{\odot}$) regime were led by Da Rio et al. (2009, 2012), while claims about the possibility of age spread within the PMS stars in the associations were reported by Da Rio et al. (2010).

Thanks to the high angular resolution and wide field achievable with the instruments on board the *Hubble Space Telescope* (*HST*), several LMC associations containing PMS candidates were identified (Gilmozzi et al. 1994; Romaniello 1998; Panagia et al. 2000; Gouliermis et al. 2006, 2007; Romaniello et al. 2006; De Marchi et al. 2010, 2017; Spezzi et al. 2012). The spatial distribution of PMS stars within LMC

Table 1
Summary of the Observations

Program ID	Date (yy mm dd)	UT (hh:mm:ss)	Filter	T_{exp} (s)
10566	2006 Mar 2	20:53:03	F555W	5200
10566	2006 Mar 6	20:59:47	F814W	5200
12872	2013 May 26	18:47:27	F658N	2718
12872	2013 May 28	03:07:15	F658N	2718
12872	2013 May 29	03:02:02	F658N	2862
12872	2013 May 30	01:20:39	F658N	2864
13009	2013 May 26	21:58:25	F658N	2753

associations shows the existence of significant substructures, as in the case of Galactic OB associations. Moreover, the locations of the detected low-mass PMS stars on color-color diagrams are found to be in excellent agreement with those of T Tauri stars with $\lesssim 2 M_{\odot}$ in young associations of the MW (Briceño et al. 2007). Gouliermis et al. (2007) analyzed the stellar content of LH 95, finding a mass distribution from bright OB stars ($\sim 7 M_{\odot}$) to faint red PMS stars ($\sim 0.3 M_{\odot}$). They found that the PMS members of this association seem to be clustered in stellar subgroups also containing a few early-type stars.

In the present paper, we study the LH 95 association, taking advantage of the *HST* photometry in three bands. In Section 2, we describe the photometric observations, while in Section 3, we address the identification of PMS candidates via their color excess, the measurement of the $H\alpha$ luminosity, and the derivation of the stellar parameters. Section 4 shows how L_{acc} and \dot{M}_{acc} are obtained from the $H\alpha$ luminosity. A general discussion about our results is provided in Section 5, while a summary and conclusions are drawn in Section 6. Appendix A provides a discussion of how stellar mass, age, and mass accretion rate change using different evolutionary tracks, while Appendix B lists the stellar and accretion parameters of the selected low-mass PMS candidates.

2. Photometric Observations

The data were collected as part of *HST* programs 10566 (PI: Gouliermis), 12872 (PI: Da Rio), and 13009 (PI: De Marchi). The LH 95 region was observed with the Wide-Field Channel (WFC) of the Advanced Camera for Surveys (ACS) in the narrowband filter F658N (centered on the $H\alpha$ line) and the wideband filters F555W and F814W, equivalent to the standard Johnson V and I bands, respectively. A log of the ACS/WFC observations is given in Table 1. A color-composite image of the region in the filters F555W and F814W is shown in Figure 1 (also see Table 2). These F555W- and F814W-band observations are among the deepest ever taken toward the LMC (see Gouliermis et al. 2007; Da Rio et al. 2009) and will allow us to photometrically explore the accretion properties for these resolved extragalactic low-mass PMS stars.

The entire data set was reduced using the package DAOPHOTII (Stetson 1987). We used more than 30 well-sampled and unsaturated sources to model the point-spread function (PSF) of all of the F555W and F814W images. We then used the task DAOPHOTII/MONTAGE to stack all of the F555W and F814W images together in order to produce a deep image cleaned of cosmic rays and detector imperfections. We used the stacked image to create a master list of sources. We accepted all objects identified at 5σ above the background. The

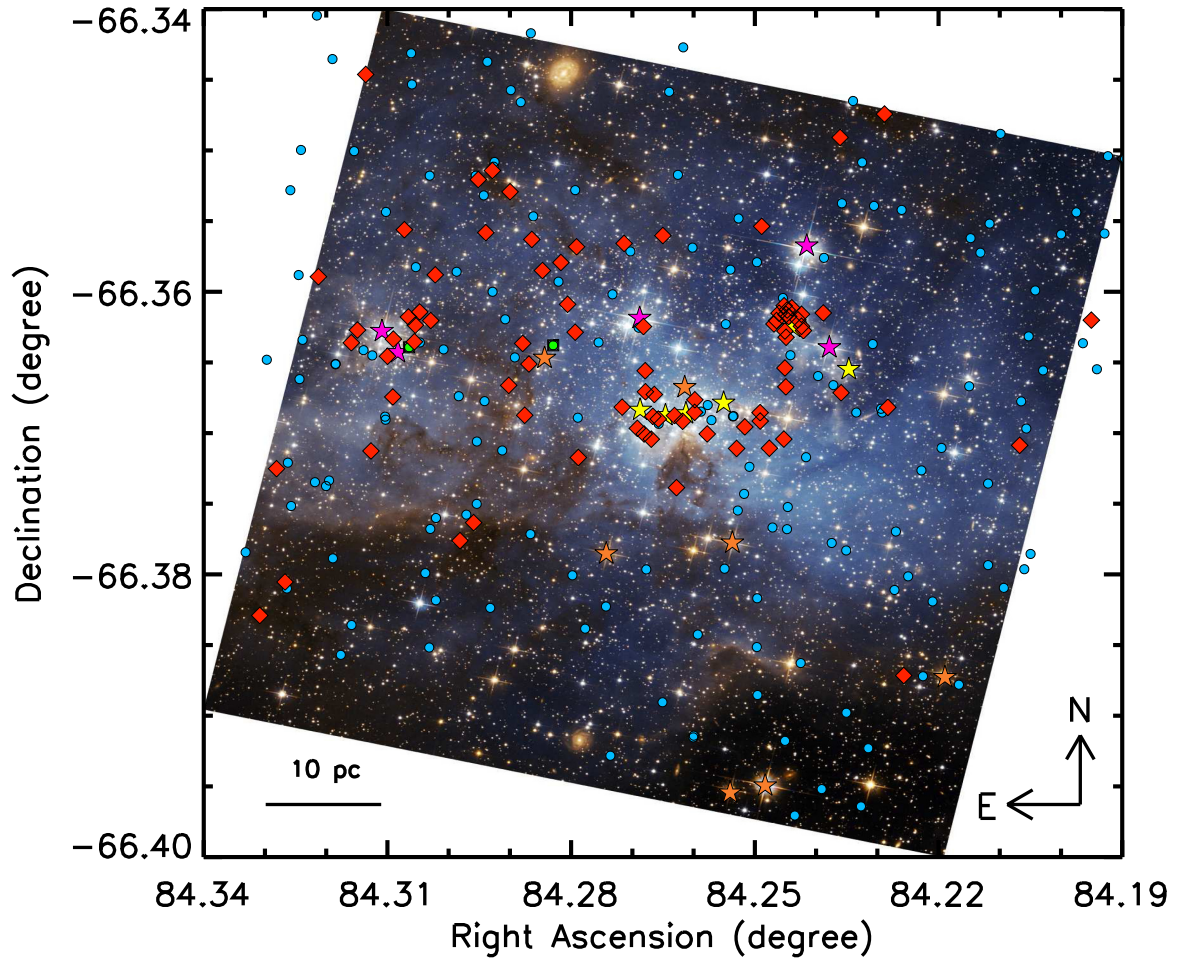


Figure 1. Color-composite image from ACS/WFC observations in the F555W and F814W filters of LH 95. Stars showing $H\alpha$ excess are displayed with filled circles and diamonds, the latter representing the younger PMS candidates; green squared circles are the two bright early-type targets excluded from our analysis (see Section 3.1 for the selection criteria of PMS candidates). Star symbols mark the position of B stars identified by Gouliermis et al. (2002; yellow), OB stars analyzed by Da Rio et al. (2012; purple), and probable massive young targets selected from the 2MASS catalog (Cutri et al. 2003) with $J - H < 0.8$ and $J < 15$ (orange). These early-type stars are listed in Table 2. North is up, and east is to the left. The field covers an area of about $0^{\circ}.15 \times 0^{\circ}.06$. (Picture credits: NASA, ESA, and the Hubble Heritage Team (STScI/AURA)–ESA/Hubble Collaboration. Acknowledgment: D. Gouliermis, Max Planck Institute for Astronomy, Heidelberg.)

master list was used to perform accurate PSF fitting photometry on each single frame using the task ALLFRAME (Stetson 1994). In order to retain a source in our final catalog, we require that the object be detected in at least three out of five images in both the F555W and F814W bands. The average of the magnitudes measured in each individual frame was adopted as the stellar magnitude, while the standard deviation was adopted as the associated photometric error.

Given the low level of stellar crowding affecting the images taken with the F658N filter, we used aperture photometry to measure the m_{658} magnitude of the stars. Aperture photometry was obtained with DAOPHOTII using five deep-drizzled images. These images are available for download as part of the high-level scientific products of the archive of the Space Telescope Science Institute (STScI). We used the catalog of sources measured in F555W and F814W as a master list of stars. We registered the position of the stars listed in this catalog on the astrometric system of the drizzled images with an overall accuracy of $0''.05$. Once again, the average of the magnitudes measured in at least three out of five frames for every master list object was adopted as the stellar m_{658} magnitude in the final catalog, while we took the resulting standard deviation around the mean for each object as the associated photometric uncertainty.

The final catalog contains 24,515 objects with measured m_{555} and m_{814} magnitudes, of which 21,512 also have a measure of m_{658} . This is expected, as the images acquired with the F658N narrow filter are slightly shallower with respect to the broadband images. We emphasize here that this is not an issue, since we are mostly interested in the identification of $H\alpha$ excess emitters, hence, stars with high flux in the F658N band.

The m_{555} , m_{814} , and m_{658} magnitudes were calibrated in the VEGAMAG system following the recipe in Sirianni et al. (2005) and using the most recent zero-point (ZP) values available through the ACS Zeropoints Calculator (Ryon 2018). As for the extinction law, we adopted the one derived specifically in the field of LH 95 by Da Rio et al. (2009). The reddening distribution obtained by the same authors does not show evidence of the patchy nature of the absorption, unlike other LMC (e.g., De Marchi et al. 2017) or nearby SFRs (see, e.g., Luhman 2007; Hillenbrand et al. 2013). Therefore, we applied a uniform reddening correction for all stars in the sample (details will be discussed in Section 3.1).

3. Data Analysis

In order to measure the $H\alpha$ luminosity, $L_{H\alpha}$, we need a solid estimate of the stellar continuum in the $H\alpha$ band, i.e., without

Table 2
Characteristics of the Early-type Stars Identified in the Field of Our Observations

Name	R.A. (hh:mm:ss)	Decl. (deg:arcmin:arcsec)	V/J (mag)
Sample of Be Stars by Gouliermis et al. (2002) ^a			
ID 114 ^b	05:37:05.38	−66:21:59.13	16.16 ^c
ID 124 ^b	05:37:04.38	−66:22:00.53	16.24 ^c
ID 157 ^b	05:36:59.33	−66:21:37.54	16.48 ^c
ID 239 ^b	05:36:57.14	−66:21:48.53	16.87 ^c
ID 410 ^b	05:37:03.57	−66:22:00.03	17.33 ^c
ID 1388 ^b	05:37:02.08	−66:21:57.29	18.53 ^c
Sample of Massive Stars by Da Rio et al. (2012) ^d			
SK-66 170	05:36:58.945	−66:21:16.130	13.17 ^c
SK-66 172	05:37:05.553	−66:21:34.950	13.58 ^c
SK-66 174	05:37:15.723	−66:21:38.355	13.74 ^c
ID 18 ^b	05:36:58.007	−66:21:42.613	14.53 ^c
ID 85 ^b	05:37:15.129	−66:21:44.304	15.58 ^c
Sample of 2MASS Stars by Cutri et al. (2003)			
2MASS J05370037−6623410	05:37:00.371	−66:23:41.03	13.254 ^c
2MASS J05365327−6623109	05:36:53.274	−66:23:10.98	14.846 ^c
2MASS J05370664−6622387	05:37:06.645	−66:22:38.73	14.212 ^c
2MASS J05370166−6622355	05:37:01.665	−66:22:35.55	14.653 ^c
2MASS J05370175−6623421	05:37:01.753	−66:23:42.15	14.554 ^c
2MASS J05370915−6621455	05:37:09.151	−66:21:45.59	14.813 ^c
2MASS J05370361−6621532	05:37:03.619	−66:21:53.22	14.848 ^c

Notes. R.A. and decl. are given in J2000.

^a These objects were classified as Be stars by Gouliermis et al. (2002) through *BVR* photometry.

^b Catalog ID number of Gouliermis et al. (2002).

^c Magnitudes in the *V* band.

^d These stars were classified as B0.2IIIp, O2III(f*)+OB, O7.5III(f), O6.5V, and B1.5III, respectively, by Da Rio et al. (2012) using high-resolution spectroscopy.

^e Magnitudes in the *J* band.

the contribution of the emission from the background. This is important for deriving the accretion luminosity and mass accretion rate, whose measurement will be discussed in the following subsections.

3.1. Identification of PMS Candidates

With the aim to identify PMS candidates within LH 95, we followed the method described and first tested in De Marchi et al. (2010) and then applied in a series of papers (Beccari et al. 2010, 2015; De Marchi et al. 2011, 2013, 2017; Spezzi et al. 2012; Zeidler et al. 2016). This method relies on the detection of H α excess emission in low-mass star-forming stars (see, e.g., Königl 1991).

We selected from our photometric catalog in the F555W, F658N, and F814W bands all those stars whose photometric uncertainties δ_{555} , δ_{658} , and δ_{814} in each individual band do not exceed 0.05 mag. A total of 1294 stars satisfy this condition (gray dots in the color–color diagram of Figure 2) out of 24,515 sources in the complete catalog (black dots in the color–magnitude diagram (CMD) of Figure 3). These stars are typically old MS and do not have appreciable H α excess; they define the reference with respect to which should look for excess emission in the $(m_{555} - m_{658})_0$ color at a given $(m_{555} - m_{814})_0$ color (see the running median represented by the dashed line in Figure 2). For comparison, this reference sequence is in good agreement with the theoretical color relationship in the same filters obtained using the Bessell et al. (1998) model

atmospheres for MS stars with effective temperature 3500 K $\leq T_{\text{eff}} \leq 40,000$ K, surface gravity $\log g = 4.5$, and metallicity index $[M/H] \simeq -0.5$ (Colucci et al. 2012), appropriate for the LMC (dotted line in the same figure). The rms deviation between the model and the data amounts to ~ 0.03 mag and is dominated by the systematic departure around $(m_{555} - m_{814})_0 \sim 1.5$, most likely due to the coarse sampling of our data. As pointed out by De Marchi et al. (2017), even before correction for reddening, such a color–color diagram provides a robust identification of stars with H α excess, since in these bands, the reddening vector runs almost parallel to the median photospheric colors of nonaccreting objects, and, moreover, our targets do not have a known patchy nature of interstellar absorption (see Da Rio et al. 2009).

To select the most probable accretors, after the exclusion of the 1294 stars taken as reference, we first selected the targets with $\delta_{555} < 0.1$, $\delta_{658} < 0.3$, and $\delta_{814} < 0.1$ mag, namely, 5155 objects. Then, we retained those whose dereddened $(m_{555} - m_{814})_0$ color exceeds the local average by at least four times the individual combined photometric uncertainty δ_3 in the three bands F555W, F658N, and F814W, where

$$\delta_3 = \sqrt{\frac{\delta_{555}^2 + \delta_{658}^2 + \delta_{814}^2}{3}}, \quad (1)$$

with δ_{555} , δ_{658} , and δ_{814} being the photometric uncertainties in each individual band. It should be noted that, for the selected

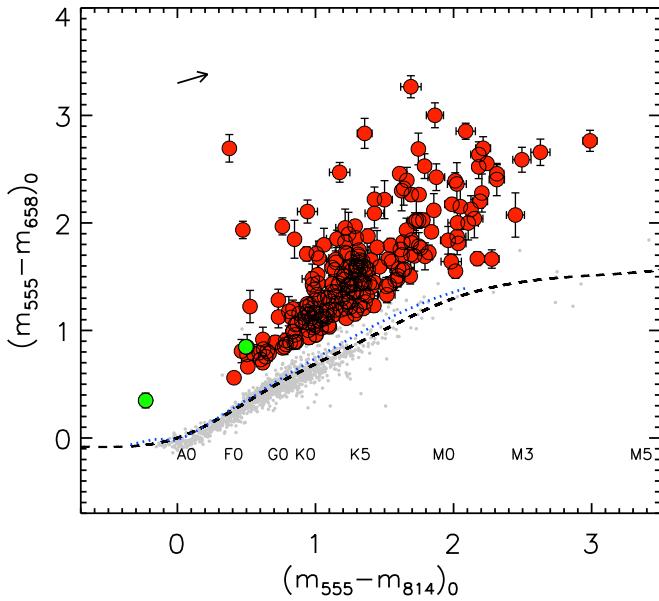


Figure 2. Dereddened color–color diagram of the selected 1541 stars in the field of LH 95. All magnitudes are already corrected for the extinction contribution of both our Galaxy and LH 95. The dashed line represents the running median photospheric $(m_{555} - m_{814})_0$ color for the 1294 stars with small (<0.05 mag) photometric uncertainties in all three bands (gray dots). The dotted line shows the model atmospheres of Bessell et al. (1998) computed for the three ACS/WFC filters. The arrow displays the reddening vector of $E(m_{555} - m_{814})^{\text{LH95}} = 0.2$ and $E(m_{555} - m_{658})^{\text{LH95}} = 0.09$ for the adopted LH 95 extinction law. A total of 247 objects with an $(m_{555} - m_{658})_0$ excess larger than 4σ are indicated with red circles. Green circles mark the positions of the two brightest ($\lesssim 22$ mag in the F555W band) targets with H α excess emission. Error bars are also shown. Spectral types as in Pecaut & Mamajek (2013) are marked at the bottom of the plot.

5155 sources, δ_3 is dominated by the uncertainty on the H α magnitude, which is, on average, around 0.15 mag, while the median value of the uncertainty in the other two bands is $\langle\delta_{555}\rangle \sim 0.03$ and $\langle\delta_{814}\rangle \sim 0.02$ mag, respectively. In the end, a total of 247 stars satisfy the condition, and they must be regarded as having a bona fide H α excess above the 4σ level (circles in Figure 2). This allows us to select the most probable PMS candidates, even when the uncertainty in the F658N band is not negligible. Indeed, as we will show in Section 3.2, our selection in H α excess emission translates directly into H α equivalent widths typical of accretors, allowing us to safely remove possible contaminants from our sample, such as chromospherically active stars (see, e.g., White & Basri 2003; Biazzo et al. 2007; Frasca et al. 2008; Beccari et al. 2015). Other classes of objects whose spectra might present H α emission are interacting binaries, but they are typically very rare in Local Group galaxies (e.g., Dobbie et al. 2014), and their intrinsic colors are bluer with respect to the MS (see, e.g., Beccari et al. 2014 and references therein).

The m_{555} magnitude versus the $m_{555} - m_{814}$ color of the detected sources is shown in Figure 3. From this CMD, the two targets with $m_{555} < 22$ are bright objects with H α excess that we exclude from the following analysis, as we are searching for low-mass PMS candidates.⁶ Gouliermis et al. (2007) found in the

⁶ Even though we could derive the parameters of these two objects from their colors, we prefer to focus only on low-mass objects. In fact, without spectroscopy, the age of these early-type stars would be rather uncertain, because they could be both PMS and post-MS stars, making the comparison with the lower-mass PMS objects of interest here more difficult.

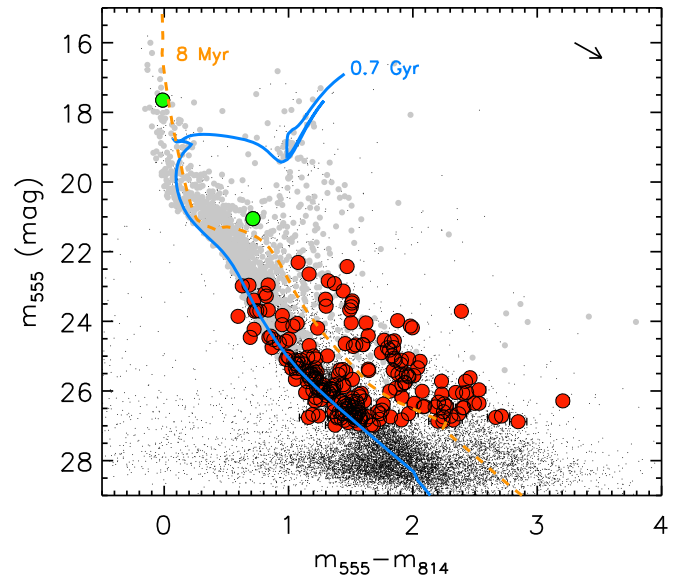


Figure 3. CMD of the field of LH 95 (24,515 sources). All magnitudes are already corrected for the extinction law of our Galaxy. As in Figure 2, green and red circles represent the 247 PMS star candidates with H α excess emission at the 4σ level with m_{555} magnitude brighter and fainter than 22 mag, respectively, while gray dots are the stars with photometric uncertainties <0.05 mag in all three filters (see text). Error bars are also shown, but they are within the symbol size in most cases. The arrow is the reddening vector of $E(m_{555} - m_{814})^{\text{LH95}} = 0.2$ and $A_{555}^{\text{LH95}} = 0.44$ applicable to LH 95. Solid and dashed lines show the theoretical isochrones from Bressan et al. (2012) for ages of 0.7 Gyr and 8 Myr, respectively; metallicity $Z = 0.007$; and a distance modulus $(m_V - M_V)_0 = 18.55$. These models only include the absorption due to our Galaxy along the line of sight (i.e., $E(m_{555} - m_{814})^{\text{MW}} = 0.1$ and $A_{555}^{\text{MW}} = 0.22$).

CMD a pronounced turnoff at $V \sim 22.5$ and a red clump (RC) at $V \sim 19$ and $V - I \sim 1.2$. The RC and old MS population are best matched by a 0.7 Gyr isochrone taken from the Padova-Trieste Stellar Evolution Code (PARSEC; see Bressan et al. 2012). Stars with H α excess are shown in red, and they define two distinct groups, nicely separated by an 8 Myr old PMS isochrone from the same authors. The theoretical isochrones of Bressan et al. (2012) are shown, with blue and orange lines in Figure 3, where the distance of 51.4 ± 1.2 kpc (Panagia 1999), corresponding to a distance modulus $(m_V - M_V)_0 = 18.55$, and a metallicity of $Z = 0.007$, typical of young LMC stars (e.g., Colucci et al. 2012), were adopted. These isochrones include both the effects of the MW intervening in absorption along the line of sight and the LH 95 mean absorption within the field. According to Fitzpatrick & Savage (1984), the former amounts to $A_{555}^{\text{MW}} = 0.22$ and $E(m_{555} - m_{814})^{\text{MW}} = 0.1$, while for the LH 95 field, we considered the following mean extinction values (Da Rio et al. 2009): $R_{555} = A_{555}/E(m_{555} - m_{814}) \simeq 2.18$ and $R_{814} = A_{814}/E(m_{555} - m_{814}) \simeq 1.18$.

To determine the presence and extent of possible differential extinction, Da Rio et al. (2009, 2012) analyzed the position of the upper-MS (UMS) stars in the CMD. In particular, after subtracting field stars, they compared the CMD position of the UMS objects with that expected according to grids of evolutionary models. They concluded that there is not a significant level of differential extinction for the UMS stars in the LH 95 field. This conclusion is very relevant to our investigation because young PMS objects and UMS stars share the same spatial distribution (see, e.g., De Marchi et al. 2011, 2013). Those authors also provided the total optical

extinction and reddening toward LH 95, namely, $A_{555}^{\text{tot}} = 0.6$ and $E(m_{555} - m_{814})^{\text{tot}} \sim 0.3$, respectively; therefore, the reddening within LH 95 is $E(m_{555} - m_{814})^{\text{LH 95}} \sim 0.2$. Finally, considering the relation $A_{658}/A_{555} \simeq 0.8$ (Rodrigo et al. 2012) and the adopted Galactic and LMC extinction laws, the total extinction in the $H\alpha$ band toward LH 95 is $A_{658} = 0.48$.

Looking at the CMD shown in Figure 3, most stars with $m_{555} - m_{814} \gtrsim 0.6$ and $m_{555} \gtrsim 22$ could be old MS or PMS objects or red giants. This is why it is important to search for PMS objects by analyzing the $H\alpha$ excess emission as a signature of accretion (and therefore of youth).

3.2. From $H\alpha$ Color Excess to Line Luminosity and Equivalent Width

As pointed out by De Marchi et al. (2010), the contribution of the $H\alpha$ line to the m_{555} magnitude is completely negligible; therefore, the magnitude $\Delta H\alpha$ corresponding to the excess emission is

$$\Delta H\alpha = (m_{555} - m_{658})^{\text{obs}} - (m_{555} - m_{658})^{\text{ref}}, \quad (2)$$

where the superscript ‘‘obs’’ refers to the observations and ‘‘ref’’ to the reference sequence at each $m_{555} - m_{814}$ color (dashed line in Figure 2). Once $\Delta H\alpha$ is derived in this way, the $H\alpha$ emission-line luminosity $L_{H\alpha}$ can be immediately obtained from the photometric ZP, the absolute sensitivity of the instrumental setup (in this case, the F658N of the ACS/WFC), and the distance to the sources. We took the F658N photometric properties of the instrument at the exact observing dates from Ryon (2018), namely, the inverse sensitivity $\text{PHOTFLAM} = 1.967 \times 10^{-18} \text{ erg cm}^{-2} \text{ s}^{-1} \text{ \AA}$, and the ZP in VEGAMAG, $\text{ZP} = 22.383$. Considering the rectangular width of the F658N filter $\text{RECTW} = 74.98 \text{ \AA}$ and assuming a distance to SN 1987A of $51.4 \pm 1.2 \text{ kpc}$ (Panagia 1999), we derived a median value of the $H\alpha$ luminosity of the 245 low-mass objects with $H\alpha$ excess of $\sim 1.2 \times 10^{31} \text{ erg s}^{-1}$ or $\sim 0.3 \times 10^{-2} L_{\odot}$. This value is lower than that measured by De Marchi et al. (2010) in the SN 1987A field ($\sim 10^{-2} L_{\odot}$) and that found by De Marchi et al. (2017) in the 30 Doradus Nebula ($\sim 3 \times 10^{-2} L_{\odot}$). This difference is not surprising because our observations include stars with greater $m_{555} - m_{814}$ colors and therefore lower masses.

The total uncertainty on our $L_{H\alpha}$ measurements is typically $\sim 16\%$ and dominated by the inaccuracy on the $H\alpha$ magnitude and the uncertainty on the distance and instrumental setup, accounting for $\sim 5\%$ and $\sim 3\%$, respectively (see also De Marchi et al. 2010). Indeed, extinction does not have any influence in the $V - H_{H\alpha}$ color excess, and therefore in the $L_{H\alpha}$ uncertainty, both because the reddening vector in Figure 2 is substantially parallel to the reference template (dashed line) and because our targets do not seem to have differential reddening, as indicated, for instance, by the relatively compact RC in the CMD.

Following De Marchi et al. (2010), the difference between the observed $H\alpha$ magnitude (m_{658}) and the level of the $H\alpha$ continuum (m_{658}^c) provides a direct measure of $\text{EW}_{H\alpha}$. In particular, since the line width is narrow compared to the width of the filter, the line profile falls completely within the filter bandpass. If we assume that the stars defining the reference template have no $H\alpha$ absorption features, their $m_{555} - m_{658}$ index would correspond to the color of the pure continuum.

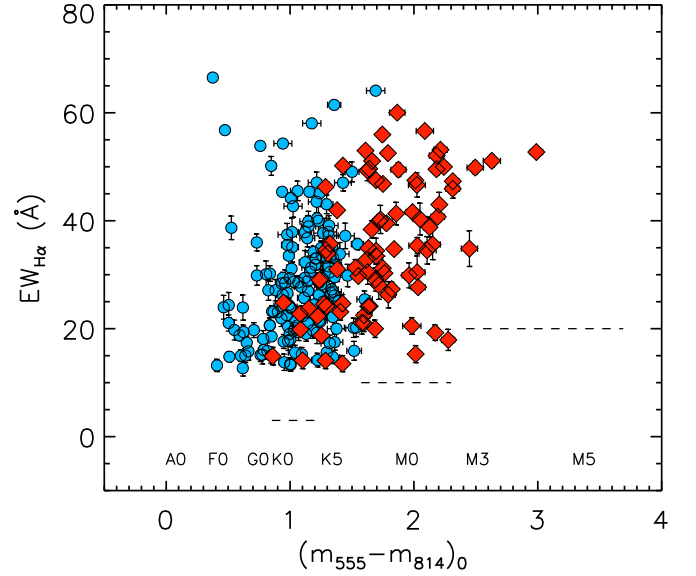


Figure 4. The $H\alpha$ equivalent width of the selected 245 low-mass PMS candidates in the field of LH 95 as a function of the dereddened $m_{555} - m_{814}$ color. The red diamonds mark the positions of the younger PMS candidates, while the blue circles represent the older PMS stars in our sample with $H\alpha$ excess (see Section 3.3 for details). Error bars are also shown. Spectral types as in Pecaut & Mamajek (2013) are marked at the bottom of the plot. Dashed lines define the thresholds above which most probable accretors are positioned at given spectral types, according to White & Basri (2003).

Therefore, $\text{EW}_{H\alpha}$ is given by the following relationship:

$$\begin{aligned} \text{EW}_{H\alpha} &= \text{RECTW} \times [1 - 10^{-0.4 \times (m_{658} - m_{658}^c)}] \\ &= \text{RECTW} \times [1 - 10^{-0.4 \times \Delta H\alpha}], \end{aligned} \quad (3)$$

with RECTW the rectangular width of the F658N filter. As for $L_{H\alpha}$, the statistical uncertainty on $\text{EW}_{H\alpha}$, typically $\sim 6\%$, is dominated by the uncertainty on the $H\alpha$ photometry. The validity of this method was also independently tested and then confirmed by Barentsen et al. (2011, 2013), who considered both photometric and spectroscopic observations for T Tauri stars in the Galactic NGC 2264 and IC 1396 young regions. The authors found a strong correlation between $H\alpha$ equivalent widths derived with both spectroscopic and photometric methods. This already suggests that the possible contribution of veiling due to accretion is greatly reduced by the subtraction of the continuum flux from the band flux.

During the last 30 yr, veiling has been more and more accurately measured, mainly thanks to spectroscopic observations of SFRs in our Galaxy (see, e.g., Hartigan et al. 1995; Manara et al. 2013; Alcalá et al. 2014, to cite a few works), but in general, its effects must also be taken into account for broadband measurements. As discussed in detail in De Marchi et al. (2010), any nebular continuum unrelated to the stellar photosphere (and therefore also the one associated with the accretion luminosity) will add to the intrinsic continuum of the stars, thereby affecting both the observed total level and the slope. This could alter the measured broadband colors of the source, thereby thwarting our attempts to infer the level of the continuum in the $H\alpha$ band from the observed m_{658} and m_{814} magnitudes and ultimately also affecting the effective temperature and bolometric luminosities that we measure (see Section 3.3.1).

Fortunately, the contribution of the nebular continuum appears to be insignificant for the stars in our sample. To prove this, De Marchi et al. (2010) assumed a fully ionized gas of pure H, considering only bound–free and free–free transitions and ignoring the contribution to the continuum from two-photon emission (Spitzer & Greenstein 1951). Using Osterbrock’s (1989, chapter 4) tabulations, they found H α line intensity and continuum fluxes of the nebular gas for gas electron temperatures in the range 5000–20,000 K (see their Table 2). The purely nebular EW $_{\text{H}\alpha}$ ranges from 5000 to 9000 Å, or more than 2 orders of magnitude higher than what we measure for our PMS objects (see Figure 4). We can, therefore, safely conclude that the nebular contribution to the continuum is negligible (less than 1%).

Furthermore, for gas temperatures in the range 5000–10,000 K, the $m_{658} - m_{814}$ color of the nebular continuum varies from 1.4 to 0.5, spanning a range typical of GK-type stars. Thus, the effects of the nebular continuum on the $m_{658} - m_{814}$ color of PMS stars remain insignificant even for the objects with the highest EW $_{\text{H}\alpha}$ in our sample. Therefore, for these objects also, the relationships between $m_{658} - m_{814}$ and effective temperature and, in turn, the bolometric luminosity that we will derive in Section 3.3.1 are not affected by the veiling introduced by the additional nebular continuum.

The values of EW $_{\text{H}\alpha}$ that we obtain in the field of LH 95 are shown in Figure 4 as a function of the dereddened $m_{555} - m_{814}$ color for the 245 low-mass PMS candidates. All selected targets at the 4σ level fall well above the threshold established by White & Basri (2003) to identify probable accretors as a function of spectral type (see also Beccari et al. 2014), thus confirming that our selection criteria of PMS candidates is cautious. Indeed, the sample that we selected must be considered as a lower limit to the number of objects with genuine H α excess. This means that most probably, we are excluding from the sample the weakly accreting PMS stars, but completeness is not the aim of this work. Instead, we are interested in studying the properties of the mass accretion process in PMS stars, and for this reason, it is important to have a solid sample of candidates.

The values of EW $_{\text{H}\alpha}$ for our sample range from ~ 12 to ~ 70 Å, with a median of 29 Å. These values are typical of PMS stars. It should be noted that, because of the width of the specific F658N filter, $\Delta\text{H}\alpha$ includes small contributions due to the emission of the two forbidden [N II] lines at 6548 and 6584 Å. De Marchi et al. (2010), following a conservative approach, estimated corrections of ~ 0.98 , on average, for the ACS F658N filter. This translates into a lower EW $_{\text{H}\alpha}$ value by ~ 0.2 – 1.4 Å in the range characteristic of our targets, i.e., within the uncertainties of our measurements (see Table 3).

3.3. Astrophysical Parameters of PMS Candidates

The physical parameters of the PMS candidates identified in Section 3.1, i.e., their effective temperature, bolometric luminosity, mass, and age, were obtained as explained in the following two subsections.

3.3.1. Effective Temperature and Bolometric Luminosity

We derived the effective temperature T_{eff} from the observed $m_{555} - m_{814}$ color, properly corrected for the total reddening due to both our Galaxy and LH 95, as explained in Section 3.1. The models of Bessell et al. (1998) with

$3500 \text{ K} \leq T_{\text{eff}} \leq 40,000 \text{ K}$, $\log g = 4.5$, and metallicity index $[\text{M}/\text{H}] = -0.5$ dex were used for the conversion from color to effective temperature, following the work by De Marchi et al. (2010) for the ACS/WFC filters (see that paper for details). Since the models of Bessell et al. (1998) are available only for $T_{\text{eff}} > 3500 \text{ K}$, for lower temperatures, we decided to consider the $T_{\text{eff}} - (V - I_C)$ calibration by Pecaut & Mamajek (2013),⁷ assuming for simplicity that the calibrated m_{555} and m_{814} magnitudes coincide with V and I_C . The reason for using a different calibration at temperatures lower than those covered by the models of Bessell et al. (1998) is to avoid possibly larger uncertainties in T_{eff} due to arbitrary extrapolations, as the relationship between T_{eff} and $m_{555} - m_{814}$ is critical for very cool temperatures. The bolometric luminosity L_* was obtained from the m_{555} magnitude corrected for the interstellar extinction (see Section 3.1), having adopted a distance to LH 95 of 51.4 kpc (Panagia 1999) and a bolometric solar magnitude $M_{\text{bol}}^{\odot} = 4.74$ (Pecaut & Mamajek 2013) and applied at any T_{eff} the bolometric corrections of the latter authors.

The positions of the PMS candidates in the H-R diagram are displayed in Figure 5, where the $\pm 1\sigma$ uncertainties on T_{eff} and L_* are also shown; in most cases, these errors are within the symbol size. They are mostly due to uncertainties in photometry and distance.⁸ As a reference, we traced the PMS theoretical isochrones of Bressan et al. (2012) for metallicity $Z = 0.007$, as appropriate for the young populations of the LMC (e.g., Colucci et al. 2012), and for ages of 1, 8, 16, and 32 Myr from right to left (dot-dashed lines). Also shown are the representative PARSEC evolutionary tracks for masses of 0.1, 0.2, 0.4, 0.6, 0.8, 1.0, 1.2, 1.5, 2.0, 3.0, and $4.0 M_{\odot}$ from the same Bressan et al. (2012) models (solid lines). The dashed line in the same figure defines the zero-age main sequence (ZAMS) by Bressan et al. (2012). From the stellar bolometric luminosity and effective temperature, we also derived the stellar radius R_* , assuming 5770 K as the effective temperature of the Sun. Typical mean uncertainties on R_* are around 5% and include both uncertainties in T_{eff} and L_* .

In the H-R diagram of our PMS candidates, a bimodal distribution in age and T_{eff} seems to be evident, with a separation around 8 Myr. In particular, stars younger than 8 Myr have a mean $T_{\text{eff}} \sim 3965 \text{ K}$, while older targets have a mean T_{eff} of $\sim 4990 \text{ K}$. This apparent bimodality will also be evident in the accretion properties, thus proving that it is not caused by detection limits. This issue will be discussed in the following sections.

3.3.2. Mass and Age

After having identified a population of PMS candidates in Section 3.1 and derived their effective temperature and bolometric luminosity in the previous subsection, it is important for our purposes to determine their mass and age from the H-R diagram (see Figure 5). We followed the approach originally discussed in Romaniello (1998) and most recently refined by De Marchi et al. (2011, 2013). The method, without making assumptions on the properties of the

⁷ We verified that in the T_{eff} range in common, the two calibrations are in very good agreement. In particular, considering the parameter space of the present work, the agreement is within ~ 0.03 mag and $\sim 70 \text{ K}$ in color and T_{eff} , respectively.

⁸ Note that uncertainties in T_{eff} and L_* do not include possible color–magnitude temporal variability due to the observations in the F555W and F814W filters having been obtained 4 days apart (see Table 1).

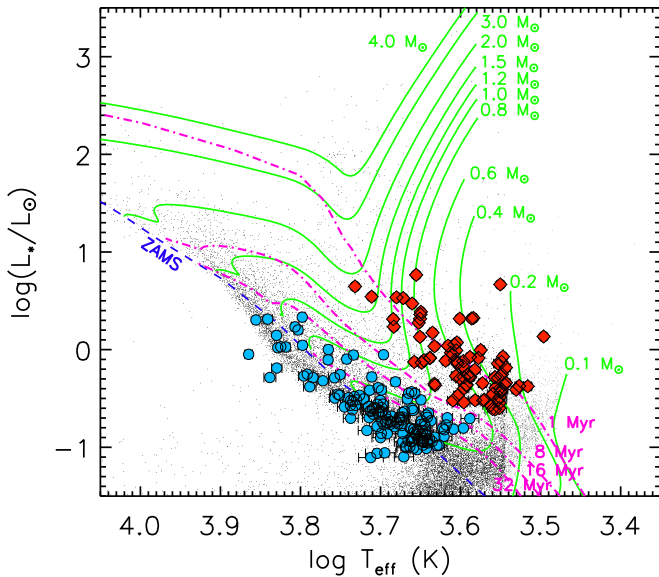


Figure 5. Location of the PMS candidates in the H-R diagram (diamonds: younger PMS stars; circles: older PMS stars). Superimposed are the PARSEC evolutionary tracks (solid green lines) and theoretical isochrones (dot-dashed magenta lines) of Bressan et al. (2012) for metallicity $Z = 0.007$. The masses in M_{\odot} and ages in Myr are indicated next to each track and isochrone, respectively. The position of the ZAMS is marked with a dashed line.

population and the pure basis of the measurement errors, provides the probability distribution for each individual star to have a given value of mass and age, with typical uncertainties of $\sim 5\%$ and $\sim 15\%$, respectively (see De Marchi et al. 2017 for a thorough explanation of the procedure). In particular, we determined the most likely mass M_* of the 245 low-mass PMS candidates of LH 95 by comparing the location of each object on the H-R diagram with theoretical PMS evolutionary tracks. As for the latter, we adopted the already mentioned PARSEC tracks for $Z = 0.007$ and available down to $M_{\odot} = 0.09 M_{\odot}$ (Bressan et al. 2012).

Comparing masses computed from different evolutionary tracks is important for the determination of the uncertainty on the mass accretion rate and its relationship with stellar mass and age. In order to assess how differences in the evolutionary models affect our results, in Appendix A, we compare mass, age, and mass accretion rate measurements obtained using the Pisa tracks from Tognelli et al. (2011), available down to $M_* = 0.2 M_{\odot}$, with those obtained using the PARSEC tracks. For an extensive discussion of the model-dependent age estimation in clusters, see the recent review by Soderblom et al. (2014).

We determined the ages of individual objects by interpolating between the isochrones in the H-R diagram. As already mentioned in Section 3.1, it is evident from Figure 5 that the PMS candidates appear to be distinct in two populations with a “gap” around 8 Myr. We thus decided to divide the sample of selected PMS candidates into two subsamples depending on their age: from now on, we will indicate as younger PMS candidates those with age $t < 8$ Myr and older PMS candidates those with $t > 8$ Myr. With such an age difference, older PMS stars must belong to a previous generation with respect to the younger PMS objects; thus, no spatial relationship (whether a correlation or anticorrelation) should be expected between the two types of objects, as is indeed evident in Figure 1. This will be discussed in more detail in Section 5.1. The younger PMS

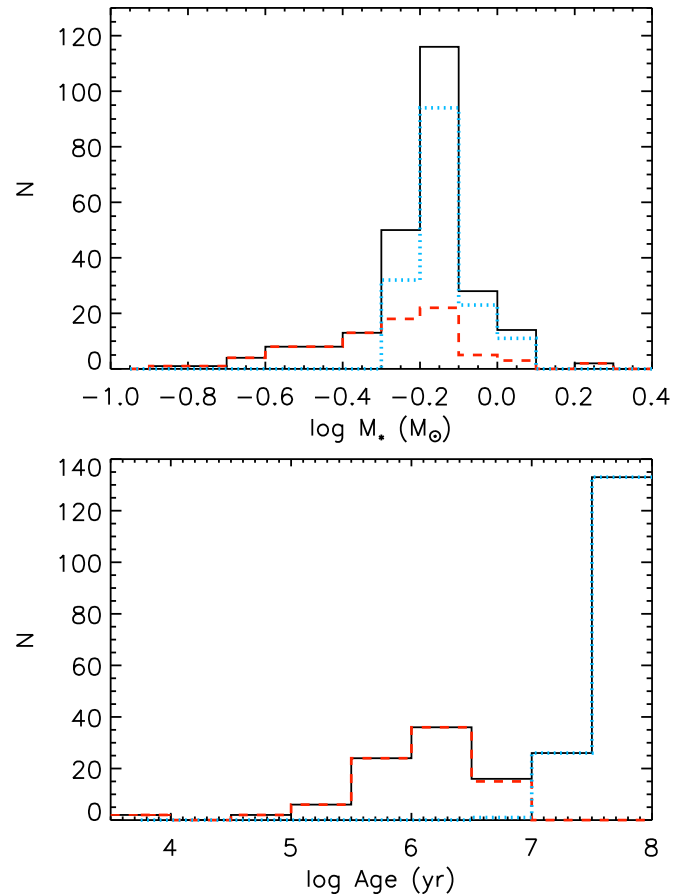


Figure 6. Histograms of the stellar mass (upper panel) and age (lower panel) for the 245 low-mass PMS candidates (solid lines). Dashed (red) and dotted (blue) lines correspond to the distributions of the younger and older populations, respectively.

candidates are about 35% (85/245) of the total sample, while the older PMS candidates represent about 65% (160/245).

The histograms with the mass and age distributions for the 245 low-mass PMS candidates are shown in Figure 6. Different line types correspond to younger (dashed lines) and older (dotted lines) PMS candidates. The mass distributions are peaked at similar values for both younger and older populations, but they show different ranges, with the younger population having a wider range in mass than the older one. Not surprisingly, old PMS stars comprise many low-mass stars, since the more massive objects have already reached the MS. Inspecting the age distribution, a clear separation between younger and older PMS stars is evident. We highlight here that these measurements are not reliable for putting constraints on the shape of the mass function or the exact value of the star formation rate, since we are only considering PMS with $H\alpha$ excess emission at the 4σ level at the time of the observations. Moreover, we are not taking into account photometric incompleteness, which is unavoidably more severe at lower masses.

As already found by De Marchi et al. (2010, 2017) in other regions of the LMC, it is noteworthy that many of the PMS candidates in Figure 5 are close to the MS and would have been missed if no information on their $H\alpha$ excess had been available. Since we would expect to find very young objects above and to the right of the MS in the CMD, it is indeed

customary to identify PMS objects by searching in that area of the CMD. However, this method of identification of PMS stars is not very reliable because of the presence of older populations and possible age spreads in the same field, which prevent the true identification of PMS stars on the basis of the stellar effective temperatures and luminosities alone (see discussion in De Marchi et al. 2010). In fact, these older PMS stars were not detected by Gouliermis et al. (2007) and were considered as field stars by the same authors.

In summary, we find evidence for a series of at least two star formation episodes, which correspond to two distinct stellar populations with different ages. We indeed identify a generation of younger PMS stars with ages ranging from <1 up to ~ 7 Myr (median value ~ 1 Myr) and a generation of older PMS stars with ages of ~ 10 – 60 Myr (median value ~ 50 Myr). Objects of this type are to be expected, also according to the evolutionary tracks. In fact, from the PARSEC tracks at metallicity $Z = 0.007$, a star with a mass of $\sim 0.7 M_{\odot}$, i.e., around the peak histogram of our sample (see Figure 6), takes ~ 50 Myr to reach the MS.

4. Accretion Properties

4.1. Accretion Luminosity

In the magnetospheric accretion scenario, the accretion luminosity can be determined from the measurement of the reradiated energy from the circumstellar gas ionized and heated by the funnel flows (e.g., Hartmann et al. 1998). The $H\alpha$ line, and hence its luminosity, generated in this process can be used as a diagnostic to derive the accretion luminosity. From the analysis of a set of $L_{H\alpha}$ measurements of a group of T Tauri stars in Taurus-Auriga compiled by Dahm (2008), De Marchi et al. (2010, 2013) found the following $L_{\text{acc}}-L_{H\alpha}$ relationship, which we adopt in this work:

$$\log L_{\text{acc}}/L_{\odot} = \log L_{H\alpha}/L_{\odot} + (1.72 \pm 0.25), \quad (4)$$

where the ratio $L_{\text{acc}}/L_{H\alpha}$ is linear. Recently, Alcalá et al. (2017), using X-shooter spectra of class II objects in the Galactic Lupus SFR, concluded that the empirical relationships they derived between L_{acc} and the luminosity of several lines from UV to NIR are consistent with being linear.

Taking into account Equation (4), the median value of the accretion luminosity thus obtained for our sample of 245 low-mass PMS candidates is $\sim 0.17 L_{\odot}$. The statistical uncertainty on L_{acc} is dominated by the quoted uncertainty of $\sim 16\%$ on $L_{H\alpha}$ mainly associated with the photometric error in the $H\alpha$ magnitude. There is also a systematic error due to the $L_{\text{acc}}-L_{H\alpha}$ relationship, but since we used Equation (4) for all PMS stars, this uncertainty will not prevent the comparison between different targets. Comparable uncertainties in the $L_{\text{acc}}-L_{H\alpha}$ relationship were obtained by Alcalá et al. (2017) for the Lupus SFR.

4.2. Mass Accretion Rate

Once L_{acc} is known, the mass accretion rate \dot{M}_{acc} can be derived from the freefall equation that links the luminosity released in the impact of the accretion flow with the rate of mass accretion according to the following relationship (see,

e.g., Hartmann 1998):

$$\dot{M}_{\text{acc}} = \left(1 - \frac{R_{\star}}{R_{\text{in}}}\right)^{-1} \frac{L_{\text{acc}} R_{\star}}{GM_{\star}} \approx 1.25 \frac{L_{\text{acc}} R_{\star}}{GM_{\star}}, \quad (5)$$

where M_{\star} and R_{\star} are the stellar mass and photospheric radius, respectively; R_{in} is the inner radius of the accretion disk; and G is the universal gravitational constant. Here R_{in} corresponds to the distance at which the disk is truncated because of the stellar magnetosphere and from which the disk gas is accreted and channeled by the magnetic field lines; therefore, its value is rather uncertain because it depends on how the accretion disk is coupled with the star. Following Gullbring et al. (1998), we assume $R_{\text{in}} = 5 R_{\star}$ for all PMS stars.

The median value of the distribution of mass accretion rates is $\sim 7.5 \times 10^{-9} M_{\odot} \text{ yr}^{-1}$, with higher values for the younger PMS candidates ($\sim 5.4 \times 10^{-8} M_{\odot} \text{ yr}^{-1}$) and lower values for the older PMS candidates ($\sim 4.8 \times 10^{-9} M_{\odot} \text{ yr}^{-1}$).

Concerning the statistical errors on \dot{M}_{acc} , the first source of uncertainty is $L_{H\alpha}$. With our selection criteria, the typical uncertainty on $L_{H\alpha}$ is $\sim 16\%$ and is dominated by random errors. The other sources of uncertainty for \dot{M}_{acc} are the stellar mass and radius. The uncertainty on R_{\star} is typically $\sim 5\%$, including the systematic uncertainty on the distance modulus. As for the mass, its determination is linked to the comparison of the location in the H-R diagram with the evolutionary tracks. When we interpolate through the PMS evolutionary tracks to estimate the mass, the uncertainties on effective temperature and stellar luminosity imply an error of $\sim 7\%$ on M_{\star} . Combining all sources of errors, the statistical uncertainty on \dot{M}_{acc} is $\sim 18\%$.⁹

The systematic uncertainty on \dot{M}_{acc} is dominated by the knowledge of the ratio $L_{\text{acc}}/L_{H\alpha}$ reported in Equation (4). As already mentioned in Section 4.1, this ratio, even if uncertain by a factor of ~ 2 due to the variations of the $H\alpha$ line intensity, is the same for all stars; therefore, the comparison between different objects is not hampered by this uncertainty, as long as the statistical errors are small (see De Marchi et al. 2010).

As pointed out by De Marchi et al. (2010), other sources of systematic errors on the derived \dot{M}_{acc} are due to theoretical evolutionary tracks and isochrones, reddening, $H\alpha$ emission generated by processes different from accretion, and contribution of nebular continuum to the photometric colors. Concerning the first source of errors, the main uncertainty on the derived mass and age comes from differences between models computed by different authors or the use of models with metallicities that might not properly describe the stellar population under study. As shown in Appendix A, if we had, for instance, used the Tognelli et al. (2011) PMS tracks instead of those of Bressan et al. (2012) at the same metallicity, we would have obtained similar values of mass and age for the PMS, to within 2% and 6%, with the largest discrepancy for $0.35 M_{\odot} \lesssim M_{\star} \lesssim 0.70 M_{\odot}$ (see Appendix A). Concerning the metallicity, had we used tracks with Z lower by 30%, the

⁹ Our observations in F555W and F814W are not simultaneous to those in F658N (see Table 1), thus implying that part of the scatter in \dot{M}_{acc} could also be due to intrinsic stellar variability. At timescales of a few years, as in our case, variations may be up to ~ 0.3 dex in $\log \dot{M}_{\text{acc}}$ (see Costigan et al. 2014). This is fully consistent with the observed 0.25 dex dispersion around the average relation between mass accretion rate and age for stars of similar mass reported by De Marchi et al. (2011). The intrinsic stellar variability of PMS candidates in several clusters of the Magellanic Clouds (including LH 95) will be the subject of a forthcoming work (G. De Marchi et al. 2019, in preparation).

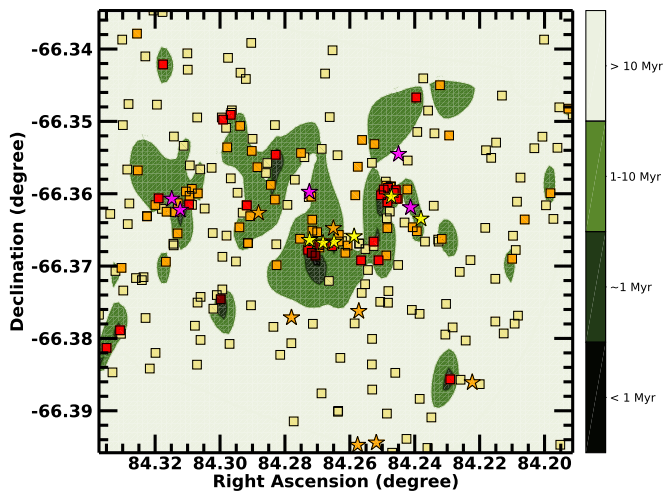


Figure 7. Spatial distribution of PMS candidates in the field of LH 95. Squares are color-coded by mass accretion rate, where more highly accreting PMS stars ($\dot{M}_{\text{acc}} \gtrsim 10^{-7} M_{\odot} \text{ yr}^{-1}$) are marked with darker red. Filled green contour regions show the position and density distribution of the PMS stars of different ages, with darker green regions corresponding to the density distribution of the youngest targets (<10 Myr), as indicated in the bar on the right. The lighter green background corresponds to the distribution of the older PMS stars with ages of some tens of 10 Myr. As in Figure 1, star symbols mark the positions of Be stars identified by Gouliermis et al. (2002; yellow), OB stars studied by Da Rio et al. (2012; purple), and probable massive young targets selected from the 2MASS catalog (Cutri et al. 2003) with $J - H < 0.8$ and $J < 15$ (orange). North is up, and east is to the left.

masses of our PMS objects would be systematically smaller by about 10% and the ages younger by a negligible amount for the luminosity and temperature ranges typical of our targets. For what concerns the reddening, we followed De Marchi et al. (2010) and concluded that underestimating the $E(m_{555} - m_{814})$ color excess by ~ 0.2 mag would lead to a 30% overestimate of R_*/M_* . This translates into the same overestimate of \dot{M}_{acc} , which is smaller than the typical measurement uncertainties in the determination of the mass accretion rate. Finally, the possibility that processes different from accretion (e.g., chromospheric activity, H knots along the line of sight, ionization of H gas from nearby massive stars) or nebular continuum may alter the determination of \dot{M}_{acc} was addressed in detail in De Marchi et al. (2010), with the conclusion that their contribution is negligible. Indeed, the contribution of the background emission was safely removed thanks to the fact that the m_{658} magnitude of each star was determined above the background calculated locally in an annulus of a few arcseconds around the centroid of the star (see also Section 2).

5. Discussion

We will now explore the distribution of the accreting PMS candidates we identified in Section 3.1, how L_{acc} depends on stellar luminosity and effective temperature, and how \dot{M}_{acc} depends on stellar mass and age. A comparison between our results and those obtained in SFRs of our Galaxy and in the LMC will also be discussed.

5.1. Spatial Distribution of Accreting PMS Stars

From a first inspection of the spatial distribution of the most probable accreting objects in LH 95 shown in Figure 1, younger low-mass PMS candidates (red diamonds) appear to be

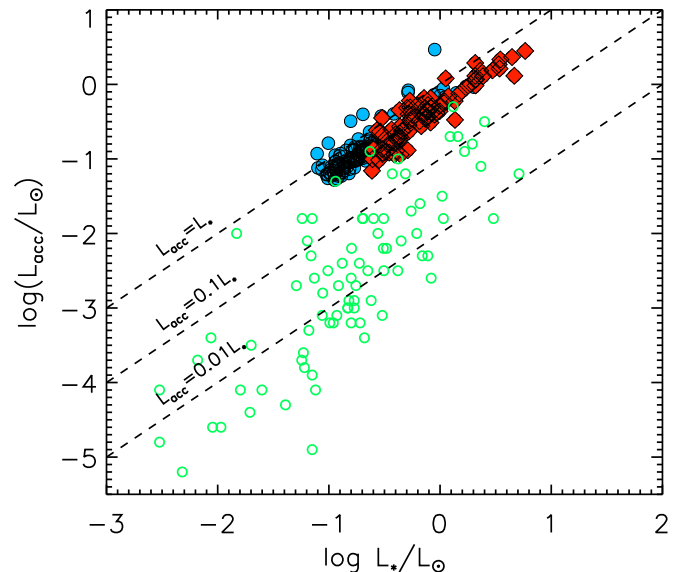


Figure 8. Accretion luminosity vs. stellar luminosity. Circles and diamonds are as in Figure 5. Dashed lines represent the loci of the three $L_{\text{acc}}-L_*$ relations, as labeled. Open circles represent the Alcalá et al. (2017) sample of low-mass stars in the Galactic Lupus SFR observed with the X-shooter spectrograph.

clustered around Be stars. In particular, they are nonuniformly distributed in the field of the LH 95 association, but they are concentrated in small clusters around bright massive stars, with a clumpy spatial distribution on the scale of ~ 5 pc. Older PMS stars do not seem to form any significant concentration and are uniformly distributed within the region. Gouliermis et al. (2007) suggested the existence of significant substructures of early-type stars containing candidate Herbig Ae/Be stars for LH95. Here we support this scenario, but we also suggest that the subgroups of early-type stars include low-mass young PMS objects, similar to Galactic OB associations, like Orion (Briceño et al. 2005, 2018).

Besides very different ages, as discussed in Section 3.3.2, the two populations of younger and older PMS stars also have considerably different spatial density distributions. We compare these distributions in Figure 7 by means of filled contours. In this figure, we considered the total population of 245 low-mass PMS candidates with well-defined masses and ages. The remarkable feature is the difference in the spatial distribution of younger and older PMS stars, with older objects much more widely distributed and not overlapping with the younger generation.

The spatial distribution of the younger and strongly accreting PMS stars in Figure 7 suggests that a recent star formation episode occurred a few Myr ago in regions also including many of the early-type Be stars identified in the LH 95 field. The older and less-accreting PMS stars are instead uniformly distributed without any specific clumping within the field. They might have formed several tens of Myr ago in a more central configuration but later had time to dissipate in a widespread configuration. Their mean age of ~ 50 Myr and spatial distribution within ~ 40 – 50 pc at the distance of LH 95 (see also Figure 1) is indeed compatible with a velocity dispersion of a few km s^{-1} , which is typical for young SFRs.

5.2. Accretion Luminosity versus Stellar Parameters

Figure 8 shows the accretion luminosity as a function of the stellar luminosity for both younger and older PMS stars. As

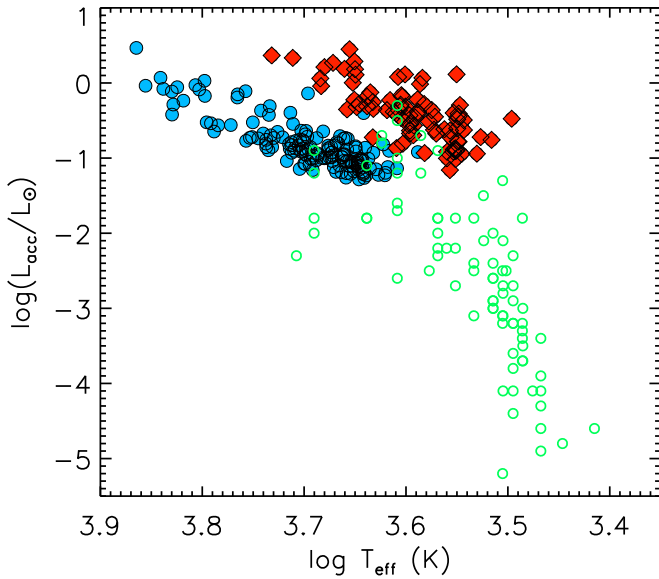


Figure 9. Accretion luminosity vs. effective temperature. Filled circles and diamonds are the same as in Figure 5. The Galactic Lupus objects by Alcalá et al. (2017) are overlaid as open circles.

already observed in SFRs close to the Sun, L_{acc} increases with stellar luminosity, with a dispersion appearing to be even smaller for our targets (the recent case of the Lupus SFR by Alcalá et al. 2017 is shown as an example). The accretion luminosity of our PMS candidates mainly falls in the range between $0.2L_*$ and $\sim L_*$, with the peak of the accretion luminosity distribution around $\sim 0.5\text{--}0.6L_*$, while those of regions in the solar neighborhood, like the Lupus SFR by Alcalá et al. (2017) superimposed in the figure, is typically $\lesssim 0.1L_*$ (see also, e.g., Muzerolle et al. 1998; White & Hillenbrand 2004; Antonucci et al. 2011; Caratti o Garatti et al. 2012; Biazzo et al. 2014). In this context, we cannot make a real quantitative comparison between our results and the findings by Alcalá et al. (2017), but it is possible that the differences between the samples could be mainly due to the following reasons: (i) different selection criteria of accreting PMS candidates; (ii) different methods to derive stellar parameters; (iii) different $L_{\text{acc}}\text{--}L_{\text{H}\alpha}$ relationships, which can lead to differences up to $\sim 0.2\text{--}0.3$ dex in $\log L_{\text{acc}}/L_{\text{H}\alpha}$ (for instance, the $L_{\text{acc}}/L_{\text{H}\alpha}$ ratio in the case of the Alcalá et al. 2017 empirical relationship is not exactly linear, as in our case); (iv) different mass and metallicity ranges, with our targets having $M_* = 0.1\text{--}1.8M_\odot$ (with a median of $\sim 0.7M_\odot$) and $Z = 0.4Z_\odot$, compared to $0.02\text{--}2.0M_\odot$ (with a median of $\sim 0.2M_\odot$) and $Z \sim Z_\odot$ for the Alcalá et al. (2017) sample; and (v) other environmental conditions, such as the gas density and contamination.

In Figure 9, the L_{acc} values are plotted in logarithmic scale as a function of the effective temperature of our PMS candidates, together with the sample of Alcalá et al. (2017). The $L_{\text{acc}}\text{--}T_{\text{eff}}$ plot appears to be very similar to the H-R diagram shown in Figure 5, with the younger and older PMS candidates well separated in T_{eff} . In the T_{eff} range between ~ 3.6 and ~ 3.7 , some Lupus targets seem to have similar $\log L_{\text{acc}}/L_\odot$ values to our PMS stars. This could be an indication of similar accretion properties at a given T_{eff} range, and therefore stellar mass. Unfortunately, we do not have many objects with very low effective temperatures (in particular with $\log T_{\text{eff}} < 3.5$) to

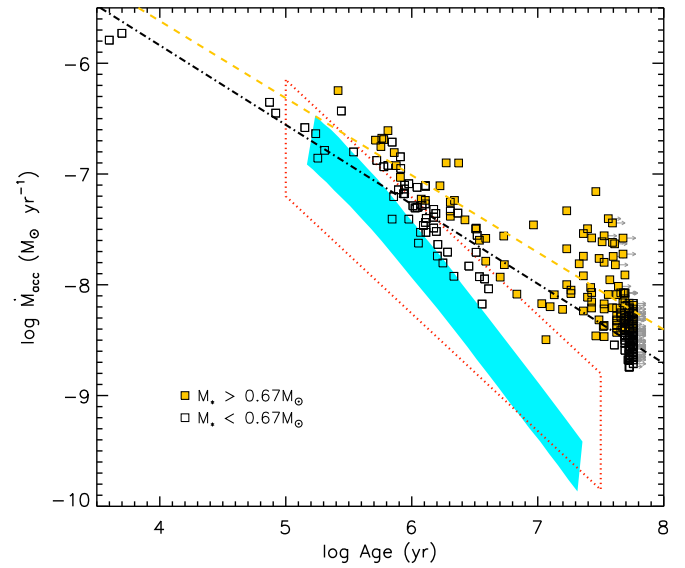


Figure 10. Mass accretion rate as a function of stellar age for our PMS candidates. The mean stellar mass is $\simeq 0.67M_\odot$. Filled and open squares represent stars with M_* larger or smaller than the mean. Regression fits for these two subsamples are represented with dashed and dot-dashed lines, respectively. Arrows indicate lower limits in stellar ages. The shaded region represents a collection of viscous disk evolutionary models taken from Hartmann et al. (1998) for solar-type stars with initial disk masses of $\sim 0.1\text{--}0.2M_\odot$, constant viscosity $\alpha = 10^{-2}$, and viscosity exponent $\gamma = 1$ (for details, see Sicilia-Aguilar et al. 2010). The dotted region shows the best linear fit and $\pm 1\sigma$ scatter obtained considering $0.3\text{--}1.0M_\odot$ stars in Galactic SFRs (see the recent review by Hartmann et al. 2016).

verify the decreasing trend observed in Alcalá et al. (2017) at the very low-mass regime.

5.3. Mass Accretion Rate versus Age

In Figure 10, the mass accretion rate is shown as a function of the stellar age. In this figure, we divided our sample into lower- and higher-mass targets, where $0.67M_\odot$ is the median mass of all PMS candidates. At first glance, the slope of the $\log \dot{M}_{\text{acc}}\text{--}\log t$ relationship appears to be similar for both lower-mass (i.e., $\simeq -0.72$) and higher-mass (i.e., $\simeq -0.70$) regimes and in good agreement with those measured in other Magellanic Cloud (MC) environments (see De Marchi et al. 2011, 2013, 2017). The shaded region in the same figure represents the prediction of viscous disk evolution by Hartmann et al. (1998). These models are able to reproduce the observed decreasing trend of \dot{M}_{acc} with age for low-mass T Tauri stars in SFRs in the solar neighborhood (see dotted region in the same figure and Hartmann et al. 2016 for a recent review of this issue¹⁰). The slope of this trend appears to be steeper than those obtained by us for both lower- and higher-mass regimes ($\simeq -1.4$ against $\simeq -0.7$). This means that in the PMS candidates of LH 95, \dot{M}_{acc} decreases more slowly with time than what is observed for low-mass T Tauri stars in Galactic SFRs close to the Sun ($\lesssim 1$ kpc; Sicilia-Aguilar et al. 2010). This behavior supports the recent suggestions by De Marchi et al. (2017), according to which, when metallicity is higher, like in the local neighborhood, there are more dust grains in the disk; therefore, the radiation pressure is higher, limiting the accretion process in both its rate and duration,

¹⁰ We note that the same authors have pointed out that this linear fit could be the consequence of correlated errors between age and accretion rate.

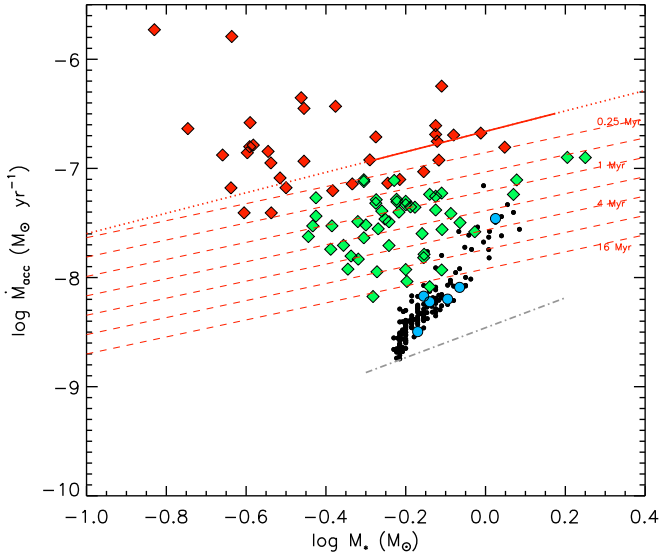


Figure 11. Mass accretion rate vs. stellar mass for the younger PMS candidates (filled diamonds) and older PMS candidates (filled circles). Colors refer to the PMS candidates with different ages (red: ≤ 1 Myr; green: 1–8 Myr; blue: 8–16 Myr; black: > 16 Myr). The solid line represents the fit to the targets younger than 1 Myr and with masses of ~ 0.5 – $1.5 M_{\odot}$ (see text), while the dotted line is the extension of this fit to lower and higher masses. Dashed lines represent the $\log \dot{M}_{\text{acc}}$ – $\log M_{\star}$ relationship obtained by De Marchi et al. (2017) at the given ages (0.25, 0.50, 1, 2, 4, 8, and 16 Myr) and considering in their Equation (3) the a and b coefficients obtained for the same mass range (0.5– $1.5 M_{\odot}$) and ages (< 16 Myr) and c coefficient obtained for 30 Doradus, which we assume to be at the same metallicity as LH 95. The dash-dotted line is the $\log \dot{M}_{\text{acc}}$ – $\log M_{\star}$ relationship obtained by Alcalá et al. (2017) for stars with $M_{\star} \sim 0.5$ – $1.5 M_{\odot}$ in the Galactic Lupus SFR.

while the mass accretion process seems to last longer at low metallicity. Other authors (e.g., Yasui et al. 2009, 2010, 2016) have concluded that in some low-metallicity environments of the outer Galaxy, the disk lifetimes are shorter than in SFRs in the solar vicinity. However, these works use the dust content of circumstellar disks as a proxy for the total mass of the disks and their lifetimes, while here we directly measure the infall of the probably more abundant gas onto the stars. Therefore, the results of the two studies are not directly comparable. And indeed, our findings are in agreement with optical spectroscopic observations of SFRs in the Galactic anticenter (Cusano et al. 2011; Kalari & Vink 2015), which indicate that a significant fraction of the young stellar objects have preserved their accretion disks, despite the low metallicity. These authors concluded that disk survival may depend not only on metallicity but also on other environmental physical conditions or properties of the central objects. Galli et al. (2015) found the following empirical relationship between disk lifetime and stellar mass: $t_{\text{disk}} = 4 \times 10^6 (M_{\star}/M_{\odot})^{0.75}$. Such a relationship was found by the authors for stars in the Taurus-Auriga association, i.e., with $Z \sim Z_{\odot}$, but similar results were previously obtained in other solar-metallicity environments (see the case of Lupus in Bertout et al. 2007). If applied to our PMS candidates, neglecting the effects due to different metallicity or binarity (to mention a few), this relationship would imply that disks around stars of $\sim 0.55 M_{\odot}$ (median mass of our younger PMS stars) survive for $t_{\text{disk}} \sim 2$ Myr, similar to the mean age of our younger population (~ 1 Myr). A disk dispersal time of the order of 2 Myr is quite at odds with the ages of the older PMS candidates, whose disks have not been totally dissipated even at several tens of Myr. We are therefore

led to believe that, unless the older episodes of star formation were much more intense than the most recent one, it is very likely that circumstellar disks live longer in these metal-poor environments.

5.4. Mass Accretion Rate versus Mass

Figure 11 shows \dot{M}_{acc} versus M_{\star} for all PMS candidates and contains several pieces of information in one graph. Younger PMS candidates are marked with diamonds (red for ages younger than 1 Myr and green for 1–8 Myr), while older PMS candidates are represented by filled circles (the targets with ages of 8–16 Myr are shown in blue, while those older than 16 Myr are in black).

From first glance, the stars in this plot appear to define a “fan-shaped” area. At a given stellar mass, we notice a wide spread in \dot{M}_{acc} for stars younger than 16 Myr. In particular, this spread in $\log \dot{M}_{\text{acc}}$ ranges from ~ 1 dex at $\sim 0.25 M_{\odot}$ up to ~ 2 dex at $\sim 0.67 M_{\odot}$, the mean mass of our targets. Splitting the sample of PMS stars in age bins, it is evident how the mass accretion rate is higher for younger stars, with mean values ranging from $\sim 2.6 \times 10^{-7} M_{\odot} \text{ yr}^{-1}$ for stars younger than 1 Myr (red diamonds), to $\sim 3.9 \times 10^{-8} M_{\odot} \text{ yr}^{-1}$ at ~ 1 –8 Myr (green diamonds), to $\sim 1.1 \times 10^{-8} M_{\odot} \text{ yr}^{-1}$ for stars with ages of ~ 8 –16 Myr (blue circles). It is also clear that the slope of the \dot{M}_{acc} – M_{\star} relationship changes according to the stellar age, ranging from ~ 0.0 for ages younger than 1 Myr, to ~ 1.0 between 1 and 8 Myr, up to ~ 4 for 8–16 Myr and older stars. Therefore, we conclude that attempting to define a relationship between \dot{M}_{acc} and M_{\star} without taking the age of the star into account can give spurious results and should be avoided.¹¹

Another result we would like to point out concerns the slope of our targets younger than 16 Myr. In Figure 11, we show with dashed lines the trends obtained at given ages (0.25, 0.50, 1, 2, 4, 8, and 16 Myr) considering the relationship between $\log \dot{M}_{\text{acc}}$ and $(\log M_{\star}, \log t)$ by De Marchi et al. (2017) and fixing as coefficients related to age and mass those obtained for the mass range 0.5– $1.5 M_{\odot}$, i.e., $a = -0.59$ and $b = 0.78$ (see their Equation (3)), and as constant c , mainly related to the metallicity, that obtained by the same authors for 30 Doradus in the LMC (i.e., $c = -3.67$; see their Table 1), which we assume to be at the same metallicity as LH 95. Considering our LH 95 targets with ages younger than 1 Myr and in the same mass range, the slope of the $\log \dot{M}_{\text{acc}}$ – $\log M_{\star}$ (~ 1 ; solid line) is similar to that obtained by De Marchi et al. (2017) for 1 Myr stars in 30 Doradus. The slope of these targets is also similar to that found by Alcalá et al. (2017) for 0.5– $1.5 M_{\odot}$ stars in the Galactic Lupus SFR at ~ 1 –3 Myr (dot-dashed line). This latter qualitative comparison seems to suggest that Galactic and extragalactic SFRs share a similar slope of the $\log \dot{M}_{\text{acc}}$ – $\log M_{\star}$ relation. Moreover, this result also implies that the age is a parameter acting on the objects we can detect, as more massive targets reach the MS faster than lower-mass objects and consequently have lower levels of H α emission, thus causing the fan shape of Figure 11. This again supports the intercorrelation between mass accretion rate, mass, and age at given surrounding environments.

¹¹ We highlight here that part of the nondetection of weakly accreting PMS candidates with high mass is due to our stringent selection (see Section 3.2).

5.5. Mass Accretion Rate versus Stellar Age and Mass in the Context of the LMC

Assuming that all stars in our sample formed under similar conditions, we can study the simultaneous dependence of \dot{M}_{acc} on both M_* and t through a multivariate least-squares fit of the type $\dot{M}_{\text{acc}} \propto t^a \times M_*^b$. Adopting this simple relationship in the mass range $0.5\text{--}1.5 M_\odot$ and for stars younger than 16 Myr, De Marchi et al. (2017) found $a \sim -0.6$ and $b \sim 1.3$ for ~ 300 stars in 30 Doradus in the LMC. If we consider the 54 objects with these characteristics in our LH 95 sample, we find $a \sim -1.1$ and $b \sim 1.3$. We are indeed cautious about this result because of the relatively few number of targets. Therefore, we now compare the mass accretion properties of the stars in LH 95 with those in several SFRs of our Galaxy and the Magellanic Clouds obtained with the same method. This provides us quantitative information on the effects of the environment during the final stages of the star formation. Following the prescriptions given by De Marchi et al. (2017), it is convenient to use a power-law dependence on mass and age, like

$$\log \dot{M}_{\text{acc}} = a \times \log \frac{t}{\text{Myr}} + b \times \log \frac{M_*}{M_\odot} + c, \quad (6)$$

where c reflects environmental effects, such as the metallicity, on the mass accretion rate. These authors studied a homogeneous sample of 1307 objects with $0.5\text{--}1.5 M_\odot$ younger than 16 Myr in six regions of the MW, LMC, and SMC and analyzed them with the same method as our targets, finding $a = -0.59 \pm 0.02$ and $b = 0.78 \pm 0.08$, respectively. Using the same values of a and b for the PMS candidates in LH 95 with the same restriction in mass and age, we derive $c = -3.54$. This latter value is consistent with the results for the two clusters in the LMC analyzed by the authors (namely, 30 Doradus and the SN1987A field) and more generally with their relationship $c = (-3.69 \pm 0.02) - (0.30 \pm 0.04) \log Z/Z_\odot$ obtained for the six clusters in the LMC, SMC, and MW (see their Table 1). In particular, our value is between -3.41 , obtained in NGC 346 (a cluster in the SMC with $Z \sim 0.002$), and -3.65 , found for the MW clusters Trumpler 14 and NGC 3603 with $Z \sim Z_\odot$. Even if we do not draw more quantitative conclusions here, our analysis confirms the importance of considering cluster metallicity, besides stellar mass and age, when mass accretion is studied in different environments. Clearly, other physical conditions (like mean gas density or local magnetic field) of the environment might have an effect on the extent and duration of the star formation process in general and the evolution of the mass accretion rate, as suggested by De Marchi et al. (2017).

6. Summary and Conclusions

We have applied a photometric detection method to reliably identify PMS candidates actively undergoing mass accretion in a resolved stellar population without requiring spectroscopic observations to the young association LH 95 in the LMC. The method combines *HST* wideband F555W and F814W photometry with narrowband F658N imaging to (i) identify stars with H α excess using the mean $m_{555} - m_{658}$ color of normal stars with very small photometric uncertainties as a reference

template of the photospheric level; (ii) convert the excess H α magnitude into luminosity and equivalent width; and (iii) derive the accretion luminosity and mass accretion rate with similar accuracy as allowed by spectral-line analysis. The main results of our study are summarized in the following items.

1. From the original photometric catalog of 24,515 sources, we extracted 1294 targets, taken as a reference for our selection of PMS candidates, as they have errors in all three bands of less than 0.05 mag. Then, we identified 245 low-mass PMS candidates as those having $m_{555} - m_{658}$ color exceeding that of the reference stars by at least four times the photometric uncertainty at the same $m_{555} - m_{814}$ color.
2. From the measured H α luminosity of these PMS candidates, we derived the accretion luminosity and, through other stellar physical parameters obtained thanks to the Bessell et al. (1998) stellar atmospheric models, Pecaut & Mamajek (2013) calibrations, and evolutionary tracks by Bressan et al. (2012), their mass accretion rates. The PMS candidates have a median value of the mass accretion rate of $\sim 7.5 \times 10^{-9} M_\odot \text{ yr}^{-1}$.
3. Within the sample of PMS candidates, we have identified two populations, which we call younger PMS candidates ($t \lesssim 8$ Myr; median age of ~ 1 Myr) and older PMS candidates ($9 \text{ Myr} \lesssim t \lesssim 60$ Myr; median age of ~ 50 Myr) with higher median values of the mass accretion rate for the former group compared to the latter ($\sim 5.4 \times 10^{-8}$ versus $\sim 4.8 \times 10^{-9} M_\odot \text{ yr}^{-1}$).
4. We have studied how the mass accretion rate changes with time as our PMS candidates approach the MS. We find that \dot{M}_{acc} decreases more slowly with time than what is predicted by models of viscous disk evolution (Hartmann et al. 1998) and observed for low-mass T Tauri stars in Galactic SFRs within 1 kpc (e.g., Sicilia-Aguilar et al. 2010; Hartmann et al. 2016). This is in line with previous findings in the Magellanic Clouds. Analyzing the $\dot{M}_{\text{acc}}\text{--}M_*$ relationship, a clear dependence on age is evident, with a slope increasing with age.
5. We have studied the relationships between mass accretion rate, stellar mass, and age, and we confirm previous findings obtained in the Magellanic Clouds, namely, that attempts to derive correlations by separately fitting the observed dependence of \dot{M}_{acc} on M_* or t may fail and introduce biases. Since these three stellar properties are intercorrelated, a proper multivariate fit is needed. Adopting a simple regression fit of the type $\dot{M}_{\text{acc}} \propto t^a \times M_*^b$ for the PMS candidates in LH95, we find $a \sim -1.1$ and $b \sim 1.3$ for the mass range $0.5\text{--}1.5 M_\odot$ and ages younger than 16 Myr. Since there is a small number of targets, we are cautious about this result; therefore, we have also compared the mass accretion properties of the PMS candidates in LH 95 with those homogeneously derived in several regions of the MW, LMC, and SMC (see next item).
6. We have applied to LH 95 the multivariate regression fit $\log \dot{M}_{\text{acc}} = a \times \log \frac{t}{\text{Myr}} + b \times \log \frac{M_*}{M_\odot} + c$ of De Marchi et al. (2017) obtained for a uniform sample of 1307 PMS stars with masses of $0.5\text{--}1.5 M_\odot$ and younger than 16 Myr contained in six different SFRs in the MW, LMC, and SMC. The c value we find for LH 95 is close

to that of the two regions in the LMC at the same metallicity (namely, 30 Doradus and the SN 1987A field). Moreover, it is lower than that achieved in lower-Z environments and higher than that found in solar-metallicity regions, thus confirming that metallicity is an important parameter to be taken into account when studying accretion properties and evolution.

7. We find that the younger PMS stars are clustered in subgroups around early-type stars (mainly B-type stars), while the older PMS stars are more uniformly distributed over the whole field of LH 95. We note that the presence of this subclustering suggests that it may have its origin in short-lived parental molecular clouds within a giant molecular cloud complex, as in the case of Galactic OB associations (see, e.g., the Orion association; Briceño et al. 2007).
8. From a morphological study of age, spatial distribution, and accretion diagnostics, we find multiple generations of stars due to at least two star formation bursts, with the most recent one occurring some Myr ago and the previous one some tens of Myr ago. The high values of \dot{M}_{acc} of the younger PMS stars and their proximity to the early-type stars suggest that their circumstellar disks have still not considerably dispersed.

Since no infrared observations are available for this region, we cannot draw any conclusions about the relationship between accretion properties and inner disk tracers. The advent of the *James Webb Space Telescope* will allow us to link mass accretion rate and grain properties. This will also be important to find information about the disk geometry and explain which mechanisms allow circumstellar disks to feed their central PMS stars for tens of Myr in a low-metallicity, low-density environment, such as the field of LH 95, and give rise to a certain level of measurable mass accretion rate. Moreover, future spectroscopic observations of the region to derive accurate metallicity from the measurement, e.g., of the [O/H] ratio are very much needed if we want to understand the different contributions of metallicity and other effects, such as the environmental gas density, on the accretion process.

We thank our referee, Prof. Gregory Herczeg, whose extensive and insightful comments have helped us to improve the presentation of this work. K.B. is grateful to the ESA for support, via its Science Visitor program, during the data analysis useful for the preparation of this paper. K.B. also thanks the Osservatorio Astronomico di Roma for the hospitality during the preparation of the paper. This work was based on observations made with the NASA/ESA *Hubble Space Telescope* and obtained from the Hubble Legacy Archive, which is a collaboration between the Space Telescope Science Institute (STScI/NASA), the Spacte Telescope European Coordinating Facility (ST-ECF/ESA), and the

Canadian Astronomy Data Centre (CADC/NRC/CSA). Some of the data presented in this paper were obtained from the Mikulski Archive for Space Telescopes (MAST). The STScI is operated by the Association of Universities for Research in Astronomy, Inc., under NASA contract NAS5-26555. This research made use of the SIMBAD database, operated at the CDS (Strasbourg, France), and data products from the Two Micron All Sky Survey, which is a joint project of the University of Massachusetts and the Infrared Processing and Analysis Center/California Institute of Technology, funded by the National Aeronautics and Space Administration and the National Science Foundation. This research has also made use of the SVO Filter Profile Service supported by the Spanish MINECO through grant AyA2014-55216.

Appendix A Mass, Age, and Mass Accretion Rate as Determined from Different Evolutionary Tracks and Isochrones

Masses and ages computed from different evolutionary tracks allow us to estimate the model-dependent uncertainty on the relationship between \dot{M}_{acc} and the stellar mass M_* and age t .

In Figure 12, we show the comparison between the masses, ages, and mass accretion rates as derived from two sets of PMS tracks for the same metallicity, namely, the PARSEC stellar evolution model (Bressan et al. 2012) and the Pisa stellar models (Tognelli et al. 2011). Filled diamonds and circles refer to younger and older stars. The largest residuals between the two sets of tracks are seen for the younger low-mass stars, while for the older stars with higher masses, the agreement is good (see panels (a) and (b)). In particular, the two sets of models differ significantly for $\log T_{\text{eff}}$ in the range ~ 3.5 – 3.6 and $\log L_*$ in the range between -0.8 and $-0.1 L_{\odot}$, which translates into the spread in M_* and \dot{M}_{acc} of young low-mass targets observed in panels (a) and (c) of Figure 12. Squares in all three panels represent the 19 PMS younger stars departing from the 1:1 relation by twice the rms difference. The T_{eff} and L_* values of these targets place them in an area of the H-R diagram where the two sets of tracks are more discrepant, probably because of different treatment of the mixing length and opacity (P. Marigo 2019, private communication). In any case, the difference in mass of these 19 targets, representing 8% of the total sample with well-determined masses and ages with both sets of tracks, affects the determination of the mass accretion rate slightly, with mean differences of about 0.2 dex in $\log M_*$ between the PARSEC and Pisa models producing at most differences of about 0.2 dex in $\log \dot{M}_{\text{acc}}$. For the rest of the sample ($\sim 92\%$), the agreement in \dot{M}_{acc} is very good (panel (c)). Similar findings were also reported by Biazzo et al. (2014) in the case of L1616/L1615, a Galactic cometary cloud in the solar vicinity.

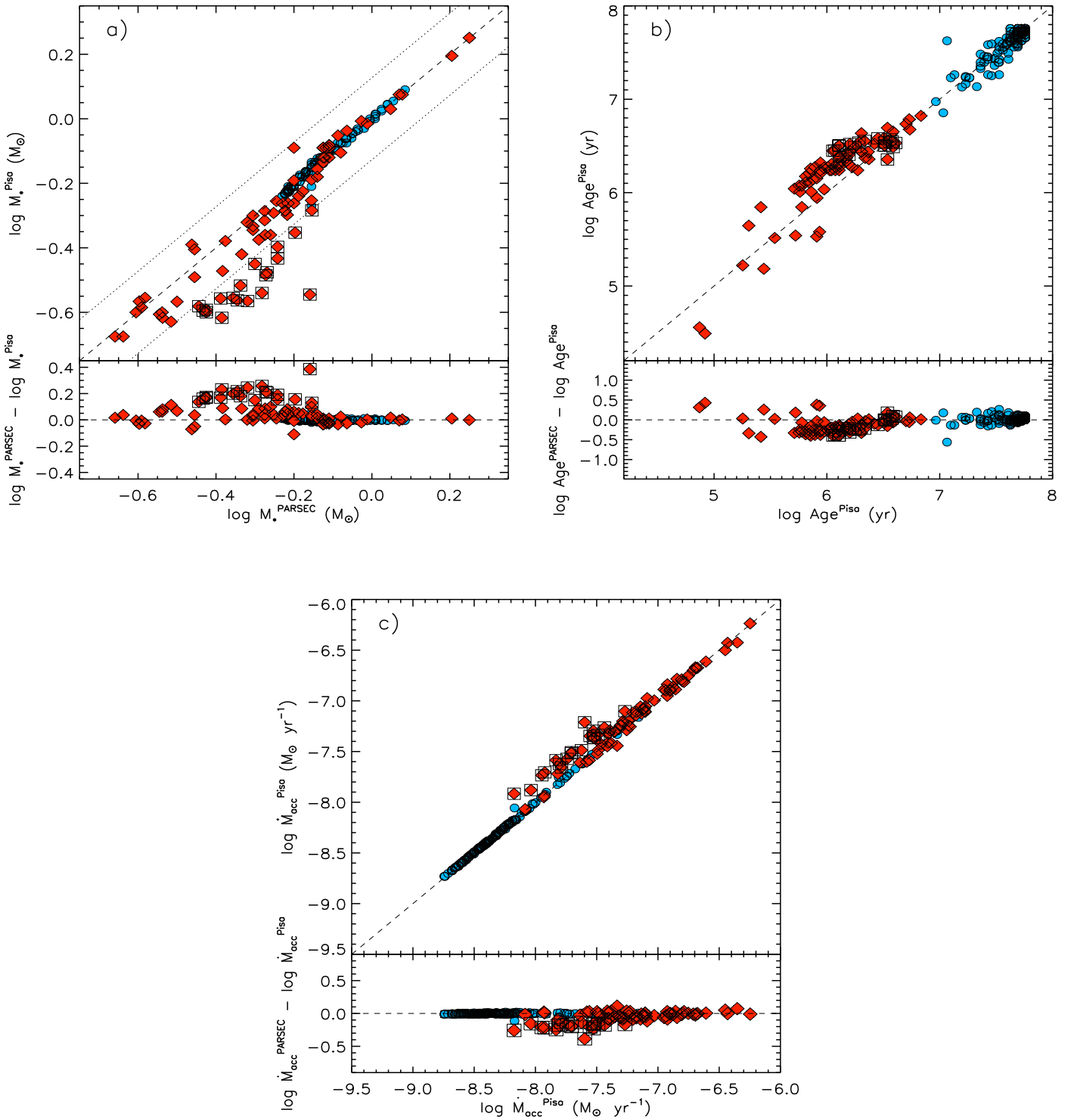


Figure 12. Comparison between masses (panel (a)), ages (panel (b)), and mass accretion rates (panel (c)) derived from the PARSEC and Pisa PMS models. Diamonds and circles refer to younger and older PMS stars. The dashed lines represent the 1:1 relation. The dotted lines in panel (a) are shifted by twice the rms difference between the $\log M_*$ values. Squares mark the positions of the targets outside the dotted lines in panel (a).





Appendix B
Stellar Parameters

Table 3
Stellar Parameters of Our Sample of PMS Accreting Candidates

Number (ID)	R.A. (deg)	Decl. (deg)	$(m_{555})_0$ (mag)	$(m_{814})_0$ (mag)	$(m_{658})_0$ (mag)	$EW_{H\alpha}$ (Å)	T_{eff} (K)	L_* (L_{\odot})	M_* (M_{\odot})	$\log t$ (yr)	$\log L_{\text{acc}}$ (L_{\odot})	$\log \dot{M}_{\text{acc}}$ ($M_{\odot} \text{ yr}^{-1}$)
Younger PMS Candidates												
100583	84.31741	-66.34244	21.873 ± 0.010	21.014 ± 0.010	20.977 ± 0.089	14.9 ± 1.5	5393 ± 29	4.44 ± 0.17	1.8	6.4	0.4	-6.9
100659	84.27160	-66.36848	21.991 ± 0.013	20.738 ± 0.011	20.773 ± 0.061	18.7 ± 1.0	4523 ± 20	5.83 ± 0.20	0.8	5.4	0.4	-6.2
101386	84.28833	-66.35663	23.130 ± 0.016	22.046 ± 0.011	21.999 ± 0.064	19.9 ± 1.0	4823 ± 28	1.71 ± 0.06	1.2	6.3	-0.0	-7.2
101473	84.29159	-66.36192	23.237 ± 0.018	21.963 ± 0.012	21.887 ± 0.079	24.6 ± 1.1	4490 ± 20	1.88 ± 0.06	0.8	5.9	0.0	-6.9
101511	84.27044	-66.36885	23.275 ± 0.020	21.103 ± 0.011	21.607 ± 0.089	19.2 ± 1.4	3551 ± 10	4.65 ± 0.13	0.2	3.6	0.1	-5.8
Older PMS Candidates												
100952	84.32237	-66.36344	22.520 ± 0.012	21.902 ± 0.013	21.820 ± 0.081	12.7 ± 1.5	6277 ± 56	2.15 ± 0.08	1.1	7.2	0.0	-7.3
100959	84.26922	-66.36774	22.528 ± 0.021	22.064 ± 0.022	21.720 ± 0.151	24.0 ± 2.2	6934 ± 92	2.05 ± 0.06	1.2	>7.6	0.1	-7.4
100973	84.29169	-66.36190	22.545 ± 0.012	22.135 ± 0.014	21.985 ± 0.064	13.2 ± 1.1	7172 ± 57	2.01 ± 0.07	1.2	>7.5	-0.0	-7.6
101478	84.32236	-66.36340	23.241 ± 0.017	22.622 ± 0.016	22.325 ± 0.161	23.9 ± 2.3	6272 ± 71	1.11 ± 0.03	1.0	>7.6	-0.2	-7.6
101503	84.32544	-66.33817	23.267 ± 0.025	22.716 ± 0.021	22.483 ± 0.115	19.8 ± 1.8	6584 ± 84	1.06 ± 0.03	1.0	>7.6	-0.2	-7.7

Notes. Columns list: object ID within our catalog; R.A.; decl.; dereddened magnitude in the F555W, F814W, and F658N bands; $H\alpha$ equivalent width; effective temperature; luminosity; mass; age; accretion luminosity; and mass accretion rate. Typical uncertainties in mass, age, $\log L_{\text{acc}}$, and $\log \dot{M}_{\text{acc}}$ are discussed in the text.
(This table is available in its entirety in machine-readable form.)

ORCID iDs

Katia Biazzo  <https://orcid.org/0000-0002-1892-2180>
 Giacomo Beccari  <https://orcid.org/0000-0002-3865-9906>
 Guido De Marchi  <https://orcid.org/0000-0001-7906-3829>
 Nino Panagia  <https://orcid.org/0000-0002-2515-5653>

References

- Alcalá, J. M., Manara, C., Natta, A., et al. 2017, *A&A*, 600, A20
 Alcalá, J. M., Natta, A., Manara, C., et al. 2014, *A&A*, 561, A2
 Antonucci, S., García-López, R., Nisini, B., et al. 2011, *A&A*, 534, 32
 Barentsen, G., Vink, J. S., Drew, J. E., et al. 2011, *MNRAS*, 415, 103
 Barentsen, G., Vink, J. S., Drew, J. E., & Sale, S. E. 2013, *MNRAS*, 429, 1981
 Beccari, G., De Marchi, G., Panagia, N., et al. 2015, *A&A*, 574, A44
 Beccari, G., De Marchi, G., Panagia, N., & Pasquini, L. 2014, *MNRAS*, 437, 2621
 Beccari, G., Spezzi, L., De Marchi, G., et al. 2010, *ApJ*, 720, 1108
 Bertout, C., Siess, L., & Cabrit, S. 2007, *A&A*, 473, L21
 Bessell, M., Castelli, F., & Plez, B. 1998, *A&A*, 333, 231
 Biazzo, K., Alcalá, J. M., Covino, E., et al. 2012, *A&A*, 547, A104
 Biazzo, K., Alcalá, J. M., Frasca, A., et al. 2014, *A&A*, 572, A84
 Biazzo, K., Frasca, A., Henry, G. W., Catalano, S., & Marilli, E. 2007, *ApJ*, 656, 474
 Bressan, A., Marigo, P., Girardi, L., et al. 2012, *MNRAS*, 427, 127
 Briceño, C., Calvet, N., Hernández, J., et al. 2005, *ApJ*, 129, 907
 Briceño, C., Calvet, N., Hernández, J., et al. 2018, *AJ*, 157, 85
 Briceño, C., Hartmann, L., Hernández, J., et al. 2007, *A&A*, 661, 1119
 Camenzind, D. 1990, *RvMA*, 3, 234
 Caratti o Garatti, A., García-López, R., Antonucci, S., et al. 2012, *A&A*, 538, A64
 Colucci, J. E., Bernstein, R. A., Cameron, S. A., & McWilliam, A. 2012, *ApJ*, 746, 29
 Costigan, G., Schözl, A., Stelzer, B., et al. 2012, *MNRAS*, 427, 1344
 Costigan, G., Vink, J. S., Schözl, A., Ray, T., & Testi, L. 2014, *MNRAS*, 440, 3444
 Cusano, F., Ripepi, V., Alcalá, J. M., et al. 2011, *MNRAS*, 410, 227
 Cutri, R. M., Skrutskie, M. F., van Dyk, S., et al. 2003, *yCat*, 2246
 Dahm, S. 2008, *AJ*, 136, 521
 Da Rio, N., Gouliermis, D., & Gennaro, M. 2010, *ApJ*, 723, 166
 Da Rio, N., Gouliermis, D., & Henning, T. 2009, *ApJ*, 696, 528
 Da Rio, N., Gouliermis, D. A., Rochau, B., et al. 2012, *MNRAS*, 422, 3356
 De Marchi, G., Beccari, G., & Panagia, N. 2013, *ApJ*, 775, 68
 De Marchi, G., Panagia, N., & Beccari, G. 2017, *ApJ*, 846, 110
 De Marchi, G., Panagia, N., & Romaniello, M. 2010, *ApJ*, 715, 1
 De Marchi, G., Panagia, N., Romaniello, M., et al. 2011, *ApJ*, 740, 11
 Dobbie, P. D., Cole, A. A., Subramaniam, A., & Keller, S. 2014, *MNRAS*, 442, 1663
 Fang, M., Kim, J. S., van Boekel, R., et al. 2013, *ApJS*, 207, 5
 Fitzpatrick, E. L., & Savage, B. D. 1984, *ApJ*, 279, 578
 Frasca, A., Biazzo, K., Taş, G., Evren, S., & Lanzafame, A. C. 2008, *A&A*, 479, 557
 Galli, P. A. B., Bertout, C., Teixeira, R., & Ducourant, C. 2015, *A&A*, 580, A26
 Gilmozzi, R., Kinney, E. K., Ewald, S. P., Panagia, N., & Romaniello, M. 1994, *ApJL*, 435, L43
 Gouliermis, D., Brandner, W., & Henning, T. 2006, *ApJL*, 636, L133
 Gouliermis, D., Keller, S. C., de Boer, K. S., Kontizas, M., & Kontizas, E. 2002, *A&A*, 381, 862
 Gouliermis, D. A., Henning, T., Brandner, W., et al. 2007, *ApJL*, 665, L27
 Gullbring, E., Hartmann, L., Briceño, C., & Calvet, N. 1998, *ApJ*, 492, 323
 Hartigan, P., Edwards, S., & Ghandour, L. 1995, *ApJ*, 452, 736
 Hartmann, L. 1998, *Accretion Processes in Star Formation* (Cambridge: Cambridge Univ. Press)
 Hartmann, L., Calvet, N., Gullbring, E., & D'Alessio, P. 1998, *ApJ*, 495, 385
 Hartmann, L., Herczeg, G., & Calvet, N. 2016, *ARA&A*, 54, 135
 Henize, K. G. 1956, *ApJS*, 2, 315
 Herczeg, G. J., & Hillenbrand, L. A. 2008, *ApJ*, 681, 594
 Hillenbrand, L. A., Hoffer, A. S., & Herczeg, G. J. 2013, *ApJ*, 146, 85
 Kalari, V. M., & Vink, J. S. 2015, *ApJ*, 800, 113
 Königl, A. 1991, *ApJS*, 370, L39
 Kontizas, M., Kontizas, E., Dapergolas, A., Argyropoulos, S., & Bellas-Velidis, Y. 1994, *A&AS*, 107, 7
 Lucke, P. B. 1974, *ApJS*, 28, 73
 Lucke, P. B., & Hodge, P. W. 1970, *AJ*, 75, 171
 Luhman, K. L. 2007, *ApJS*, 173, 104
 Manara, C. F., Beccari, G., Da Rio, N., et al. 2013, *A&A*, 558, A114
 Manara, C. F., Testi, L., Herczeg, G. J., et al. 2017, *A&A*, 604, A127
 Mulders, G. D., Pascucci, I., Manara, C. F., et al. 2017, *ApJ*, 847, 31
 Muzerolle, J., Hartmann, L., & Calvet, N. 1998, *AJ*, 116, 2965
 Osterbrock, D. 1989, *Astrophysics of Gaseous Nebulae and Active Galactic Nuclei* (Mill Valley, CA: Univ. Science Books)
 Panagia, N. 1999, in *IAU Symp. 190, New Views of the Magellanic Clouds*, ed. Y.-H. Chu et al. (Cambridge: Cambridge Univ. Press), 549
 Panagia, N., Romaniello, M., Scuderi, S., & Kirshner, R. P. 2000, *ApJ*, 539, 197
 Pecaut, M. J., & Mamajek, E. E. 2013, *ApJS*, 208, 9
 Rigliaco, E., Natta, A., Randich, S., Testi, L., & Biazzo, K. 2011, *A&A*, 525, 47
 Rodrigo, C., Solano, E., & Bayo, A. 2012, *IVOA Working Draft, SVO Filter Profile Service v1.0*, Tech. Rep. 1015 (Baltimore, MD: International Virtual Observatory Alliance)
 Romaniello, M. 1998, PhD thesis, Scuola Normale Superiore di Pisa
 Romaniello, M., Scuderi, S., Panagia, N., Salerno, R. M., & Blanco, C. 2006, *A&A*, 446, 955
 Rosotti, G. P., Clarke, C. J., Manara, C. F., & Facchini, S. 2017, *MNRAS*, 468, 1631
 Ryon, J. E. 2018, *ACS Instrument Handbook, Version 17.0* (Baltimore: STScI), <http://www.stsci.edu/hst/acs/documents/handbooks/current/cover.html>
 Sicilia-Aguilar, A., Henning, T., & Hartmann, L. W. 2010, *ApJ*, 710, 597
 Sirianni, M., Jee, M. J., Benítez, N., et al. 2005, *PASP*, 117, 1049
 Soderblom, D. R., Hillenbrand, L. A., Jeffries, R. D., Mamajek, E. E., & Naylor, T. 2014, in *Protostars and Planets VI*, ed. H. Beuther et al. (Tucson, AZ: Univ. Arizona Press), 219
 Spezzi, L., De Marchi, G., Panagia, N., Sicilia-Aguilar, S., & Ercolano, B. 2012, *MNRAS*, 421, 78
 Spitzer, L., Jr. & Greenstein, J. L. 1951, *ApJ*, 114, 407
 Stetson, P. B. 1987, *PASP*, 99, 191
 Stetson, P. B. 1994, *PASP*, 106, 250
 Tognelli, E., Prada Moroni, P. G., & Degl'Innocenti, S. 2011, *A&A*, 533, A109
 Vorobyov, E. I., & Basu, S. 2009, *ApJ*, 703, 922
 White, R. J., & Basri, G. 2003, *ApJ*, 582, 1109
 White, R. J., & Hillenbrand, L. A. 2004, *ApJ*, 616, 998
 Yasui, C., Kobayashi, N., Saito, M., & Izumi, N. 2016, *ApJ*, 151, 115
 Yasui, C., Kobayashi, N., Tokunaga, A. T., Saito, M., & Tokoku, C. 2009, *ApJ*, 705, 54
 Yasui, C., Kobayashi, N., Tokunaga, A. T., Saito, M., & Tokoku, C. 2010, *ApJL*, 723, L113
 Zeidler, P., Grebel, E. K., Nota, A., et al. 2016, *ApJ*, 152, 84